

Trần Quốc Khuê

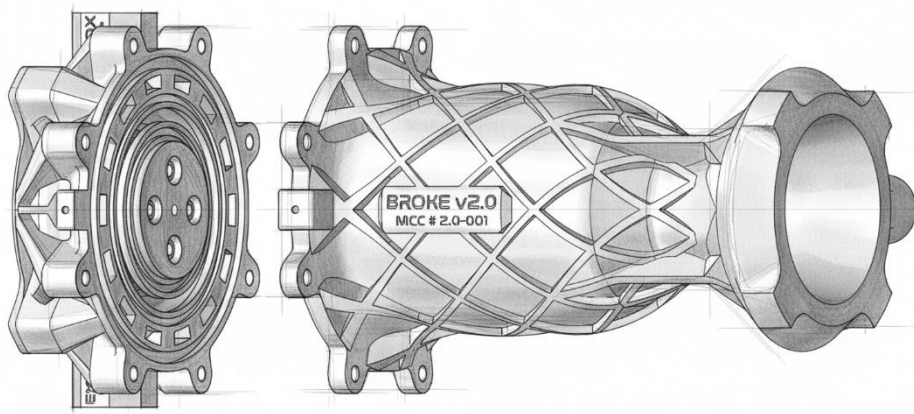
# Development of BROKE 2

An Additively Manufactured, High-Performance,  
Cost-Optimized 1.2kN LOX-Ethanol Rocket Engine

Bachelor Thesis in Mechanical Engineering

Supervisor: Dr. Trần Trung Thành

September 2025



**Budget Rocket Engine**



QR Code for Digital Report

# Development of BROKE 2:

An Additively Manufactured, High-Performance, Cost-Optimized  
1.2kN LOX-Ethanol Rocket Engine

Trần Quốc Khuê  
Supervisor: Dr. Trần Trung Thành

Vietnamese-German University

September 2025

This page is intentionally left blank.

## **Acknowledgement**

First, I would like to thank my family and friends for their unwavering support throughout this challenging project and my ambiguous life.

I am deeply grateful to my supervisor, Dr. Tran Trung Thanh, for his guidance and encouragement during the course of this thesis. I also wish to thank the machine shop teams who assisted in the manufacturing of the rocket engine.

Special thanks go to my friends at The Exploration Company for their support during my Propulsion Design Internship. I truly appreciated the great times and valuable experiences we shared together.

## Abstract

This thesis presents the design, analysis, and manufacturing of a 1.2 kN regeneratively cooled LOX–Ethanol rocket engine – the BROKE-2 engine. The engine features an advanced cooling system, comprising double-pass cooling channels, and an additively manufactured AlSi<sub>10</sub>Mg combustion chamber optimized for both performance and cost.

Numerical analyses, including CFD and FEA, were conducted to assess cooling effectiveness and structural integrity under steady-state conditions. The results confirm safe operating margins with maximum wall temperatures below 230 °C and bulk stresses within the material yield limit.

Design-for-manufacturing principles were applied to ensure machinability for both additive manufacturing and post-processing operations. Although full hot-fire testing and validation are pending, the assembled prototype demonstrates the practical feasibility of developing a high-performance, low-cost engine using locally available resources.

## Tóm tắt

Luận văn này trình bày quá trình thiết kế, phân tích và chế tạo một động cơ tên lửa sử dụng nhiên liệu LOX–Ethanol có lực đẩy 1,2 kN, được làm mát tái sinh và phát triển dưới tên gọi BROKE-2. Động cơ được trang bị hệ thống làm mát tiên tiến với các kênh làm mát hai vòng, cùng buồng đốt chế tạo bằng công nghệ in 3D vật liệu AlSi<sub>10</sub>Mg, được tối ưu hóa nhằm đạt hiệu suất cao với chi phí hợp lý.

Các phân tích số, bao gồm mô phỏng CFD và FEA, được thực hiện để đánh giá hiệu quả làm mát và độ bền kết cấu trong điều kiện hoạt động ổn định. Kết quả cho thấy động cơ làm việc trong giới hạn an toàn, với nhiệt độ thành buồng đốt tối đa dưới 230 °C và ứng suất tổng thể nằm trong giới hạn chảy của vật liệu.

Các nguyên tắc thiết kế cho sản xuất (DfM) được áp dụng nhằm đảm bảo khả năng gia công cho cả quá trình in 3D và các công đoạn hoàn thiện. Mặc dù quá trình thử nghiệm đốt vẫn đang được chuẩn bị, nguyên mẫu hoàn chỉnh đã chứng minh tính khả thi của việc phát triển một động cơ hiệu suất cao, chi phí thấp, có thể chế tạo bằng nguồn lực sẵn có tại địa phương.

# Contents

<b>1</b>	<b>Introduction</b>	<b>1</b>
1.1	What does BROKE stand for? . . . . .	1
1.2	Background and motivation . . . . .	1
1.3	Objectives . . . . .	2
1.4	Document organization . . . . .	2
<b>2</b>	<b>System Architecture and Requirements</b>	<b>3</b>
2.1	Mission and operational envelope . . . . .	3
2.2	How to achieve high performance? . . . . .	3
2.3	What is flight-ready? . . . . .	4
2.4	Propellant selection and properties . . . . .	5
2.5	System constraints . . . . .	6
2.6	Design point summary . . . . .	8
2.7	Engine subsystems . . . . .	9
<b>3</b>	<b>Design for Manufacturing</b>	<b>13</b>
3.1	System Constraints Influencing Manufacturability . . . . .	13
3.1.1	Material Selections . . . . .	13
3.1.2	Foreign Object Damage (FOD) Mitigation . . . . .	13
3.2	Accessible Manufacturing Methods . . . . .	13
3.2.1	Manual Labor Work . . . . .	14
3.2.2	CNC Machining . . . . .	16
3.2.3	Additive Manufacturing . . . . .	18
3.2.4	Unconventional Machining . . . . .	20
3.3	Expected manufacturing processes . . . . .	20
3.4	Experimental Validation of Additive Manufacturing . . . . .	20
3.4.1	BROKE 2 test section . . . . .	25
3.5	SLM Additive Manufacturing Specific DfM . . . . .	29
3.6	Lessons learned . . . . .	30
<b>4</b>	<b>Main Combustion Chamber (MCC)</b>	<b>31</b>
4.1	Material Selection . . . . .	31
4.2	de Laval Nozzle Contour Profiling . . . . .	32
4.2.1	Geometry Study with a Simplified Conical Nozzle . . . . .	32
4.2.2	Empirical design parameter study . . . . .	34

## Contents

4.2.3	Summarization of MCC design points and the main internal contour . . . . .	36
4.3	Regenerative cooling circuit analysis . . . . .	38
4.3.1	Introduction . . . . .	38
4.3.2	Challenges . . . . .	38
4.3.3	BROKE 2 Regenerative Cooling Circuit Features . . . . .	46
4.3.4	Analysis methods . . . . .	51
4.3.5	Cooling analysis results . . . . .	56
4.3.6	Final cooling configurations . . . . .	68
4.4	Structure Analysis . . . . .	68
4.5	Design-for-Manufacturing Features . . . . .	72
4.6	Final Main Combustion Chamber Design . . . . .	73
<b>5</b>	<b>Final Conclusion</b>	<b>77</b>
<b>Bibliography</b>		<b>79</b>

# Chapter 1

## Introduction

### 1.1 What does BROKE stand for?

BROKE stands for **B**udget **R**Ocket **E**ngine. Yes, it is a real acronym, and yes, it also describes my bank account. The name is both an objective and a warning: build a liquid rocket engine on a tight budget, survive perpetual lack of funds, and, if I am being honest, expect the occasional mishap where something actually broke. If you think it is a joke, you are not entirely wrong.

### 1.2 Background and motivation

#### Why a small-scale liquid propellant rocket engine?

- Steep and rewarding learning curve: Designing, building, and testing a small-scale liquid engine offers a hands-on, multidisciplinary challenge. The process is engaging and educational, requiring knowledge of thermodynamics, fluid mechanics, materials, electronics, and control systems. While other rocket engine types (e.g., solid or hybrid) have their own complexities, liquid engines offer a unique opportunity to learn advanced engineering concepts in a compact and manageable format.
- High performance potential: Liquid engines can achieve higher specific impulse and efficiency compared to most solid or hybrid engines. Their performance can be tailored through propellant selection, injector design, and cooling strategies, making them ideal for research and demonstration projects.
- Controllability: Liquid engines are inherently throttleable and restartable, allowing for precise control of thrust and multiple ignition cycles. This flexibility is valuable for testing, iterative development, and applications requiring variable thrust profiles.
- Safety and legality: Small-scale liquid engines, when designed and operated with proper safety protocols, can be safer than larger systems or some solid propellant engines. They also tend to be more compliant with legal and regulatory requirements for amateur rocketry, as propellants are often less hazardous and easier to source, store, and handle.

### Complexity of objectives vs resource constraints

While ambitious objectives are important, it is essential to remain realistic about the constraints faced in a student thesis project. Cost and time limitations inevitably shape the scope and complexity of the engine design. In practice, these constraints lead to several key trade-offs:

- Reduced thrust output: The engine is sized for laboratory demonstration or potential integration with a small-scale vehicle, rather than large payload capability.
- Moderate chamber pressure: Operating at relatively low chamber pressures reduces structural and thermal demands, thereby simplifying both analysis and testing.
- Pressure-fed cycle: A pressure-fed architecture is adopted to avoid the complexity, cost, and reliability challenges associated with pumps.

These trade-offs allow for a manageable project scope while still providing valuable learning experiences in liquid rocket engine design, fabrication, and testing.

## 1.3 Objectives

The objective of this thesis is to design and document a liquid rocket engine demonstrator that balances technical performance with practical manufacturability and adaptability. Although the thrust level is modest for a liquid rocket engine due to resource constraints, the project seeks to realize a design that is efficient, robust, and well-engineered within its class.

### Scope, limitations, and deliverables of the thesis

The scope of this thesis is limited to the design, analysis, and fabrication of a pressure-fed liquid rocket engine demonstrator. This work is intended purely for static-fire ground testing, though flight applications are considered. The primary deliverables for this project include the complete computer-aided design (CAD) package, supporting computational fluid dynamics (CFD) and finite element analysis (FEA) reports, the fully manufactured engine assembly, and a detailed test plan.

## 1.4 Document organization

This document is intended for:

- Those seeking to understand the fundamentals of rocket engine design. This thesis covers some basic hand calculation design steps.
- Engineers aiming to replicate the design process for a similar engine. Detailed design considerations and analyses are provided, especially in chapters focused on individual components.
- Operators and maintainers who require reference material for integration, operation, or maintenance of this specific engine. A dedicated chapter addresses interfacing, control, and assembly guidance.

# Chapter 2

# System Architecture and Requirements

## 2.1 Mission and operational envelope

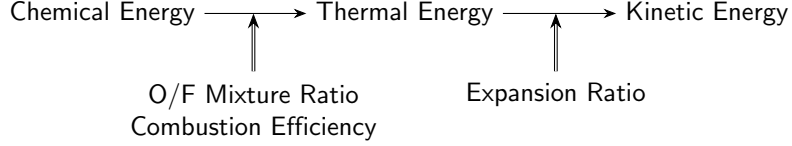
The BROKE engine is a small-scale, high-performance liquid bipropellant rocket engine designed for both ground testing and flight demonstration. The primary mission objectives are to validate the design and manufacturing process, confirm engine performance through individual component tests, static hot-fire tests, and demonstrate flight capability in a real-world environment.

- **Design and validation of manufacturing capabilities:** This phase includes designing the engines, developing manufacturing processes, manufacturing-quality control, and assembling the final engine.
- **Individual component testing:** Each major subsystem (injector, combustion chamber, nozzle, cooling system) will be tested individually to verify performance against design specifications. This includes cold-flow tests for the injector and cooling channels, hot-fire tests for the Augmented Spark Igniter (ASI).
- **Static Hot-Fire Testing:** The engine will undergo a series of static hot-fire tests to measure thrust, specific impulse, combustion efficiency, and thermal performance. These tests will validate the design and provide data for further optimization.
- **Flight Demonstration:** Following successful ground tests, the engine will be integrated into a small-scale rocket vehicle for flight demonstration. This will showcase the engine's reliability and performance in real-world conditions.

## 2.2 How to achieve high performance?

Rocket engines, like other thermal engines, operate by converting chemical energy stored in propellants into heat through combustion, and then transforming that heat into kinetic energy.

Specifically, the engine burns propellants to produce high-temperature, high-pressure gases with low velocity. These gases are then expanded through the nozzle, resulting in lower temperature,



(ideally) ambient pressure, but very high velocity exhaust. The momentum change of this exhaust produces thrust.

Achieving high performance in a rocket engine depends on maximizing two key energy conversion steps:

1. **Chemical → Heat:** Efficient combustion releases as much heat as possible from the chemical energy. This is improved by:
  - Operating near the stoichiometric mixture ratio for maximum energy release
  - Enhancing combustion efficiency through effective mixing and atomization
2. **Heat → Mechanical Energy:** Efficient expansion of hot gases into kinetic energy. This requires a high expansion ratio, which is achieved by:
  - High chamber pressure (limited by feed system constraints)
  - Low ambient pressure (not possible for ground testing)

For this engine, due to the pressure-fed cycle, it's impractical to reach high chamber pressure. Therefore, the design focuses on maximizing the chemical-to-heat conversion by optimizing the mixture ratio and combustion efficiency.

In conclusion, the engine achieves high performance through:

- Operation near the optimal oxidizer/fuel ratio maximizes energy release. The resulting high flame temperature is managed by an advanced regenerative cooling system.
- A swirl coaxial injector ensures fine atomization and thorough mixing, significantly improving combustion efficiency.

## 2.3 What is flight-ready?

### Compact engine layout and packaging

The engine is designed with a minimal footprint, with all interfaces (propellant inlets, mounting points, instrumentation ports) clearly defined to facilitate later integration with test stands and flight vehicles.

### Augmented Spark Igniter

Test bench engines usually require external ignition sources, such as pyrotechnic devices, which may not be suitable for flight applications due to added complexity and lack of restart capability. The BROKE engine employs an Augmented Spark Igniter (ASI), an integrated ignition subsystem, making it suitable for both ground and flight applications.

### Test bench to vehicle adaptation

The test bench is designed with components that can be directly transferred to flight hardware, including propellant tanks, valves, and pressure-reducing regulators. These components are selected to be compact, lightweight, and robust enough for flight, while remaining suitable for ground testing.

## 2.4 Propellant selection and properties

The selected propellants are liquid oxygen (LOX) and Ethanol. This combination was chosen for several key reasons:

1. **Ease of handling:** Ethanol and LOX are non-toxic and environmentally friendly, simplifying handling and ground operations.
2. **Availability and cost:** Both LOX and Ethanol are widely available and relatively inexpensive, making them ideal for research-focused engines.
3. **Optimized mixture for cooling:** Using LOX and Ethanol shifts the mixture toward a higher fuel fraction, enhancing regenerative cooling as more fuel absorbs heat from the chamber walls. This is evident in the table below, where LOX/Ethanol has a lower optimal O/F ratio, meaning more fuel is available for cooling.
4. **Low dynamic viscosity:** Ethanol's lower viscosity (1.074 mPa·s at 20°C) compared to IPA (2.038 mPa·s at 20°C) improves flow through cooling channels, enhancing heat transfer and reducing pressure losses. For reference, water has a viscosity of 1.002 mPa·s at 20°C.
5. **High boiling point:** Ethanol's boiling point at 20 bar is about 178°C, which allows significant heat absorption while remaining in the sub-cooled liquid region.
6. **Matched volumetric flow rates:** Selecting a mixture ratio near optimal yields nearly equal volumetric flow rates for LOX and ethanol, simplifying tank and plumbing design. For LOX ( $\approx 1.14 \text{ g}\cdot\text{cm}^{-3}$ ) and ethanol ( $\approx 0.79 \text{ g}\cdot\text{cm}^{-3}$ ) the density ratio is  $\approx 1.44$ , so choosing a mass O/F near 1.4–1.5 yields near-matching volumetric flows and enables a common approach to plumbing, pressurization, and valve sizing.
7. **Good performance:** The LOX-ethanol mixture offers competitive  $I_{sp}$  values compared to other common propellant pairs.

Propellant Pair	Optimal O/F	Theoretical Isp (s)
LOX / Ethanol	~1.67	260–265
LOX / RP-1	~2.8	270–285
LOX / IPA	~1.7	255–260
N <sub>2</sub> O / Ethanol	~6.5	230–240

Table 2.1: Performance comparison of propellant pairs. Isp values at sea level.

## 2.5 System constraints

### Engine pressure limit

The propellant tanks are seamless aluminum pressure vessels. Although they are not part of the engine itself, they impose the principal system constraint because the propulsion system is pressure-fed. The tanks' maximum allowable pressure is 35 bar, which bounds the chamber pressure once feed system losses are accounted for.

$$\begin{aligned} P_{\text{tank}} = & P_{\text{chamber}} + \Delta P_{\text{injector}} + \Delta P_{\text{regencooling}} \\ & + \Delta P_{\text{feed}} + \Delta P_{\text{regulator}} + \Delta P_{\text{margin}} \end{aligned}$$

Based on seamless aluminum tank tests and empirical pressure drop estimates:

$$\begin{aligned} \max P_{\text{tank}} &= 35 \text{ bar} \\ \Delta P_{\text{injector}} &= \frac{1}{3} \cdot P_{\text{chamber}} \\ \Delta P_{\text{regencooling}} &= 2.5 \text{ bar} \\ \Delta P_{\text{feed}} &= 0.5 \text{ bar} \\ \Delta P_{\text{regulator}} &= 0.5 \text{ bar} \\ \Delta P_{\text{margin}} &= 1.0 \text{ bar} \\ \Rightarrow P_{\text{chamber}} &= 21 \text{ bar} \end{aligned}$$

Therefore, in the pressure-fed configuration, the chamber pressure is limited to  $\approx 21$  bar.

For future electric-pump development, the required motor/shaft power (accounting for pump efficiency) is estimated below:

$$P [\text{kW}] = \dot{m} \left[ \frac{\text{kg}}{\text{s}} \right] \cdot \Delta p [\text{bar}] \cdot \frac{1}{10} \cdot \frac{1}{\eta}$$

Where  $\Delta p$  is the pressure rise provided by the pump, and  $\eta$  is the pump efficiency. Assume  $\eta$  to be 40%, and ambient pressure to be 1 bar. Therefore, in case of LOX pump:

$$P_{\text{LOX}} = 0.3 \left[ \frac{\text{kg}}{\text{s}} \right] \cdot (29 - 1) [\text{bar}] \cdot \frac{1}{10} \cdot \frac{1}{40\%} = 2.1 \text{kW}$$

And in case of Ethanol pump:

$$P_{\text{Ethanol}} = 0.2 \left[ \frac{\text{kg}}{\text{s}} \right] \cdot (32 - 1) [\text{bar}] \cdot \frac{1}{10} \cdot \frac{1}{40\%} = 1.55 \text{kW}$$

Commercial off-the-shelf brushless motors, such as 4092-series RC units, rated at 4.2 kW peak, provide a comfortable performance margin for prototype pumps (separate LOX and Ethanol pumps) development.

### Mass flow limit

In a pressure-fed cycle, practical limitations arise from the feed system hardware. The pressure regulator is expected to be the primary bottleneck, with performance constrained by:

- Pressure drop versus flow rate characteristics
- Choked flow conditions resulting from gas compressibility

For the present engine, the total propellant mass flow is approximately 0.50 kg/s, divided into 0.30 kg/s LOX and 0.20 kg/s ethanol (O/F  $\approx$  1.5 by mass). The corresponding volumetric flow rates are:

$$\dot{V}_{LOX} = 1.1410.30 \approx 0.263 \text{ L/s} \quad \dot{V}_{Ethanol} = 0.7890.20 \approx 0.253 \text{ L/s}$$

Both are below 0.30 L/s, ensuring compatibility with standard pressure-reducing regulators and plumbing capacities.

In contrast, an electric pump cycle is not subject to these gas-dynamic limitations. In that case, both flow rate and pressure head are determined directly by pump performance, as outlined in the previous paragraph.

### **Structural constraints**

The target static thrust is limited to <2 kN. This cap simplifies ground support design, allowing the test stand to be constructed from commercial aluminum extrusions while maintaining adequate safety margins.

### **Manufacturing constraints**

As a consequence of having a low thrust engine, some features, e.g. cooling channels or flow orifices, are difficult to manufacture. This later requires design tradeoffs to ensure manufacturability with available resources, such as CNC milling and 3D printing.

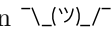
### **Budget constraints**

Major system costs are driven by propellant handling hardware: seamless aluminum tanks, pressure reducing regulators, 1/2" plumbing and fittings, and safety devices. By limiting chamber pressure, mass flow, and thrust, the design remains compatible with widely available commercial-off-the-shelf components, reducing both development costs and lead time.

### **Other non-technical constraints**

This project is funded, designed, manufactured, and tested by a **single student**—me. That means I have to do everything: design every single component, build the test bench, wire up the electronics, build custom PCBs, program the custom control stack, manufacture all the parts, procure every piece of equipment, assemble the engine, run the tests, analyze the data, and write the reports.

If it sounds overwhelming, that is because it is. To survive, I have been drinking a lot of coffee and energy drinks, but whatever efforts I pay for the project, it is still a one-man project, and the design still includes shortcuts and workarounds based on personal experience and empirical methods.

In the end, it is engineering, and risks must be taken 

### **Thrust vector control delayed development**

The engine incorporates a thrust frame structure in this design iteration, providing a foundation for future thrust vector control (TVC) integration. Due to current budget and schedule constraints, the initial prototype will not include TVC hardware. However, the modular thrust frame enables straightforward addition of gimbaling capabilities in subsequent development phases.

## 2.6 Design point summary

Design Point	Value	Note
Cycle	Pressure-fed	
Chamber pressure	21 bar	$\approx 300$ psi
Total mass flow rate $\dot{m}$	0.5 kg/s	
Propellants	LOX/Ethanol	
Mixture ratio (O/F)	1.5	By mass
Optimum ambient pressure	0.7 atm	
Estimated ISP	240 s	Sea level
Thrust	1.2 kN	Sea level
Static fire burn duration	> 20s	
Cooling method	Regenerative with supplementary film cooling	
Injector type	Swirl coaxial	
Thrust vector control	Not included in this iteration	
Ignition method	Augmented spark igniter	

Table 2.2: Design point summary for BROKE engine.

## 2.7 Engine subsystems

### Engine subsystems breakdown: final BROKE engine

The vehicle or test bench fuel supply system is responsible for delivering high-pressure propellants to the engine when pumps are not present. This external system is not considered part of the engine's subsystems; only components directly involved in combustion, cooling, and thrust generation are included within the engine subsystems boundary. Propellant management remains the responsibility of the test bench or external supply system.

The rationale for separating engine functions into dedicated subsystems is rooted in simplicity, reliability, and practicality:

- Each subsystem is assigned a single, well-defined function within the engine. This modular approach makes troubleshooting, testing, and future upgrades much easier.
- While a monolithic engine design (e.g., 3D-printing the Injector Head and Main Combustion Chamber as a single part) could eliminate seals and reduce some failure points, it is not adopted here because:
  - The technology is not mature enough for reliable depowdering and post-processing.
  - Modular components are easier to inspect, maintain, and swap out for iterative testing.
  - Assembly and inspection are more straightforward with separate parts, reducing risk and complexity.

Subsystem	Function
Main Combustion Chamber (MCC)	Generating and accelerating combusted gases
Injector Head (IH)	Propellant atomization and mixing
Augmented Spark Igniter (ASI)	Reliable ignition of propellants
Thrust Frame (TF)	Structural support and load transfer

Table 2.3: Primary subsystems of the BROKE engine.

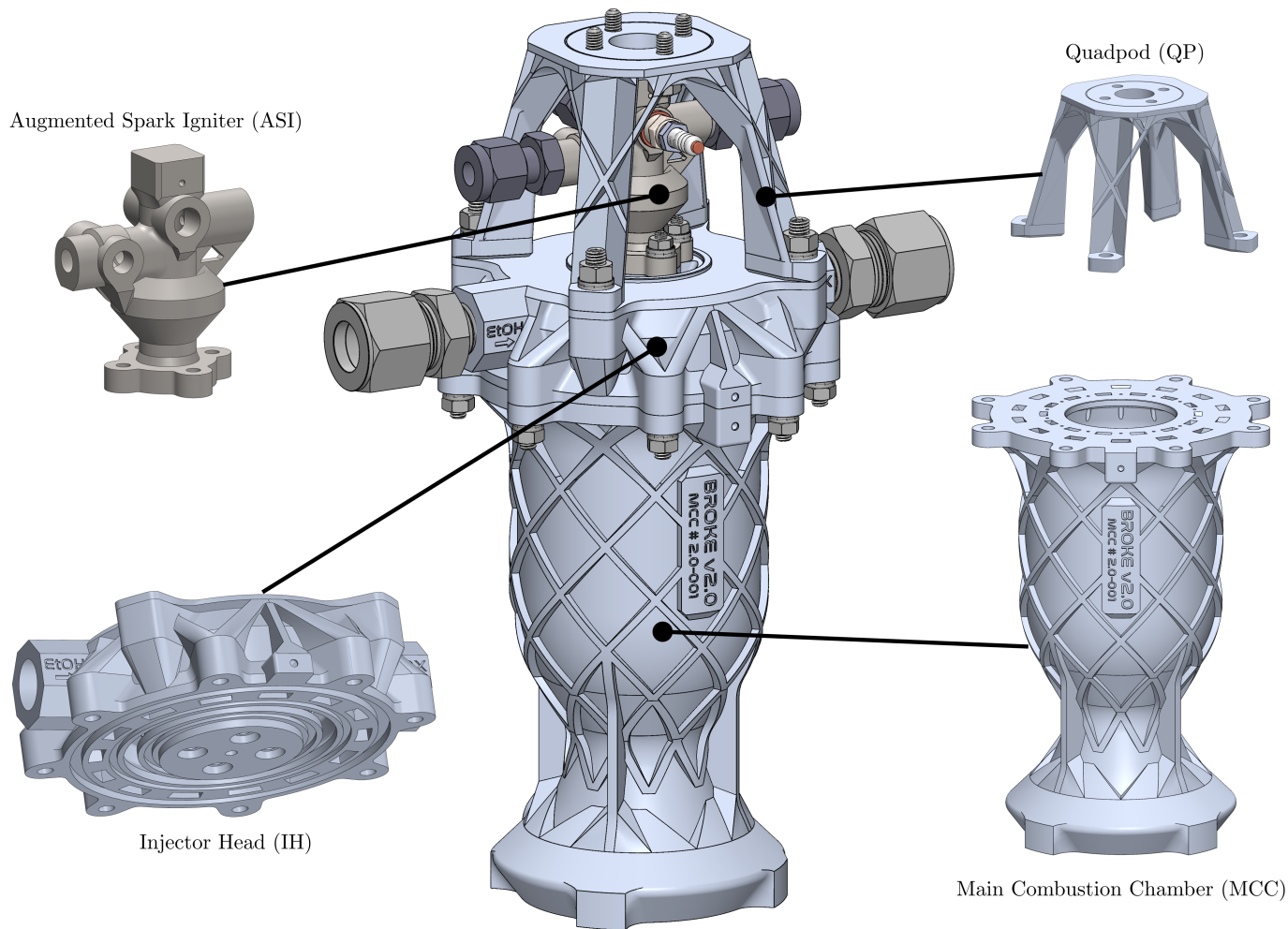


Figure 2.1: Final BROKE engine assembly with major subsystems labeled

**Engine subsystems descriptors: final BROKE engine**

While Table 2.3 summarizes the primary subsystems of the engine, this section provides a brief description of each, focusing on their functional roles and interactions at the architectural level.

**Main Combustion Chamber (MCC)**

The Main Combustion Chamber (MCC) is the core of the propulsion system, where chemical energy is converted into high-temperature, high-pressure exhaust gases. Its internal contour dictates the thermodynamic efficiency of the expansion process, while its walls must survive extreme heat fluxes through effective thermal management. The MCC is therefore the subsystem most tightly coupled to the overall engine performance and reliability.

**Injector Head (IH)**

The Injector Head (IH) introduces and atomizes the oxidizer and fuel into the combustion chamber. In addition to distributing the propellants at the desired oxidizer-to-fuel ratio, the injector creates a controlled pressure drop that contributes to combustion stability. The efficiency of atomization and mixing directly affects the combustion efficiency of the engine.

**Augmented Spark Igniter (ASI)**

The Augmented Spark Igniter (ASI) provides the initial energy required to reliably ignite the propellant mixture inside the MCC. The augmentation principle—combining a spark discharge with a pilot propellant flow—ensures ignition probability across a range of operating conditions. Its design must balance electrical, thermal, and fluidic requirements in a compact unit.

**Quadpod**

The quadpod serves as the structural backbone of the engine. It transfers axial loads generated in the MCC to the ground test stand or vehicle structure, while maintaining precise alignment between subsystems. The thrust frame also provides mounting points for sensors, feed lines, and electrical connections.

**Subsystem Interactions**

In operation, the subsystems function as an integrated sequence: propellants enter through the Injector Head, are atomized and mixed, and are then ignited by the ASI to establish stable combustion within the MCC. The resulting thrust is transmitted to the environment through the Thrust Frame. Although the design philosophy follows a modular approach for maintainability and testability, the interfaces are designed for compact and robust integration.

This page is intentionally left blank.

# Chapter 3

# Design for Manufacturing

## 3.1 System Constraints Influencing Manufacturability

### 3.1.1 Material Selections

This section discusses material choices from a manufacturing perspective, focusing on machinability, cost, availability, and Technology-Readiness-Level (TRL). Performance-related trade-offs (e.g., thermal conductivity, strength at elevated temperature) are considered later in the component-specific design sections.

This material choice is limited to metals, as they are the only materials suitable for high-temperature, high-pressure rocket engine parts. Plastics used for non-critical applications are discussed in the later Fused-Deposition-Modeling (FDM) subsection below.

Due to major budget constraints, the project is limited to Aluminum AlSi<sub>10</sub>Mg and Stainless Steel 316L for all components. Both materials are affordable, well-suited for machining, and have established additive manufacturing processes.

The selection of materials for specific components is discussed in the respective design sections.

### 3.1.2 Foreign Object Damage (FOD) Mitigation

Foreign object damage (FOD) and contamination are important concerns during designing, manufacturing, and assembly, especially for components exposed to liquid oxygen or high-pressure flow. Chips, residual powder, or traces of machining oil can lead to blockages, leaks, or even ignition. The tables below summarize typical contaminant types, associated risks, and cleaning or mitigation methods used in this project.

The large debris has its own challenge: it can one-way block the cooling channels and orifices

## 3.2 Accessible Manufacturing Methods

This subsection outlines the manufacturing methods considered practical and accessible for this project. Rather than describing the processes in general, the focus here is on *why* each method is suitable for specific components or manufacturing steps of the engine.

Material	Subtractive Manufacturing	Additive Manufacturing	Relative Cost
Aluminum AlSi <sub>10</sub> Mg	Excellent (easy cutting, low tool wear)	High maturity, widely used in SLM	Low
Aluminum 6061	Excellent (easy cutting, low tool wear)	Low TRL; prone to porosity and cracking	Low
Stainless Steel 316L	Moderate (work hardening, slower cutting)	High maturity and repeatable results	Medium
Titanium Ti <sub>6</sub> Al <sub>4</sub> V	Difficult (high tool wear, low feed rate)	High maturity, stable AM process	High
Inconel 718	Very difficult (severe tool wear, low productivity)	High maturity, dense prints achievable	High
Copper alloy	Very difficult (high tool wear, poor machinability)	Low maturity, limited supplier selections	Very High

Table 3.1: Summary of material manufacturability and relative cost.

Type	Mechanical Risk	Combustibility Risk
Large debris	High — can damage walls and surfaces, clog cooling channels and orifices	Low — typically inert metallic particles
Fine powder	Moderate — may accumulate in small orifices or channels	Medium — can promote ignition in an oxygen-rich environment
Flammable contamination	None mechanically	High — oils and greases can cause a highly combustible mixture in an oxygen-rich environment

Table 3.2: Sources and mitigation methods for potential contaminants (continued).

### 3.2.1 Manual Labor Work

#### Hand tapping

Hand tapping is particularly useful for additively manufactured parts, where printed holes may not be perfectly aligned or sized. CNC tapping requires a rigid setup with accurate datums and referencing to keep the tap concentric with the hole. This rigidity, while beneficial for precision, also makes the process unforgiving — even small misalignments between the printed hole and the tool can lead to tap breakage or part damage.

Hand tapping, on the other hand, adds a degree of flexibility. The machinist can feel the thread engagement and let the tap self-center within the printed hole, compensating for small errors in position or orientation. This makes it a safer and more practical approach for finishing threads in

Type	Source	Mitigation methods
Large debris	Machining chips, burrs	<ul style="list-style-type: none"> <li>• Shake-off or centrifuge if possible</li> <li>• Compressed-air blow</li> <li>• Water flushing</li> </ul>
Fine powder	Residual powder from additive manufacturing process	<ul style="list-style-type: none"> <li>• Ultrasonic bath</li> <li>• Compressed-air blow</li> <li>• Water flushing</li> </ul>
Flammable contamination	Cutting oils, machining coolants, handling residues	<ul style="list-style-type: none"> <li>• Degreaser wash</li> <li>• Ultrasonic cleaning</li> <li>• Water rinse and drying</li> </ul>

Table 3.3: Sources and mitigation methods for potential contaminants.

AM parts or prototypes where perfect referencing is hard to achieve.

For this project, an electric tapping arm was used instead of fully manual tapping. This approach combines the flexibility of hand tapping with practical benefits: it is less labor-intensive and provides a more consistent feed rate. The tapping arm is also equipped with a torque limiter, which helps prevent tool overload and reduces the chance of chip jamming.



Figure 3.1: Electric tapping arm

However, this does not mean that hand tapping is inherently better. When the part is properly fixtured, set up, and referenced — with the printed holes re-machined in the same CNC setup — CNC tapping remains the preferred method for accuracy and repeatability. The case of CNC tapping is discussed later in the CNC machining section.

### Deburring

Hand deburring provides similar advantages to hand tapping — flexibility and adaptability to complex geometries. For simple features such as holes, threads, or straight edges, deburring scrapers are typically used. For more complex contours or internal transitions, a rotary Dremel tool is more effective.

To protect critical surfaces during this process, sensitive areas are covered with Kapton tape to prevent accidental scratches or loss of surface finish. This simple precaution is especially important for sealing faces or polished areas that are difficult to rework.

### Polishing

This polishing step is used to eliminate small scratches on the sealing surface, and also to remove fingerprints and organic substances.

## 3.2.2 CNC Machining

The machining was under close supervision from the project author, with every step carefully double-checked. This oversight was essential due to the high precision required for CNC operations, the significant mass of material removed, and the need to utilize fixture features integrated during the design phase.

The complexity of coordinating multiple machining operations—each with unique risks and requirements—demanded thorough verification of setups, tool paths, and intermediate results to ensure dimensional accuracy and prevent errors.

This was especially critical for additively manufactured (AM) parts produced under the BROKE project budget, which were new to the local machine shops and presented unfamiliar risks. These components required careful handling and a deep understanding of their unique characteristics—since even a minor scratch or mistake could result in the loss of parts worth **hundreds or thousands of dollars**. Extra supervision ensured machinists were aware of these requirements and that all operations were performed with the necessary caution.

### Vertical-Machining-Center 3-axis milling

All critical external surfaces and features were machined on a 3-axis Vertical Machining Center (VMC).

- **Face milling:** Used to create reference surfaces and ensure parallelism of mating planes.
- **End milling:** Applied for pocketing, contouring, and precise hole resizing (e.g., re-machining printed holes).
- **Rigid tapping:** Utilized for threaded holes produced within the same coordinated setup as the machined hole features, ensuring thread concentricity and perpendicularity relative to the surrounding surfaces. Other tapping methods are less suitable: thread milling requires dedicated tooling and programming effort, while thread rolling demands tight control of pilot-hole tolerances and material ductility.

In the case of rigid tapping, the pilot holes were end-milled to enlarge the printed holes to the required sizes for tapping. By performing both the hole enlargement and tapping in the same CNC

setup, the process ensures that the threads are perfectly aligned and concentric with the surrounding machined surfaces. This approach minimizes the risk of misalignment or eccentricity that could occur if the holes were machined and tapped in separate setups.

The 3-axis milling operations were performed in a local commercial machine shop under sponsorship, with experienced machinists who also worked on the CAM programs.



Figure 3.2: 3-axis Vertical Machining Center (VMC). The MCC can be seen fixtured on the table.

### 5-axis milling

5-axis milling was considered for this project, as it offers the ability to machine multiple geometries in a single setup, reducing the need for multiple setups and re-fixture. This capability is particularly beneficial for complex parts with intricate features or tight tolerances.

Also, the 5-axis milling machine was equipped with a Renishaw probe, which allows for reference feature measurement, especially for complex geometry from additively manufactured parts.

The machine was available in the university machine shop, but due to limited access time, it was the last resort option if the 3-axis VMC could not achieve the required geometry.



Figure 3.3: 5-axis milling machine at the university machine shop.

### 3.2.3 Additive Manufacturing

#### Fused Deposition Modeling (FDM)

While plastics are not suitable for high-temperature, high-pressure rocket engine parts, they are still useful for non-critical applications such as:

- Physical visualization of parts
- Prototyping sections/features for cold flow tests, fit-checks, or assembly trials (FDM printing can replicate SLM printed parts)
- Creating fixtures or jigs for assembly or machining

- Fabricating non-structural components such as protective covers, caps, or housings



Figure 3.4: Plastic test prints

For this project, the main FDM plastics considered are PLA, PETG, and ABS, selected for their wide availability. Their key properties are summarized below for practical selection:

Note: Material strength is not a critical concern for FDM plastic parts in this project, but heat resistance is important for components exposed to elevated temperatures during operation or testing.

For plastic prints, a personally owned FDM printer (Bambulab P1S) was used. The DfM guidelines for plastic FDM printing are well-established and widely available online. Some reading resources are listed in the references section.

### Selective Laser Melting (SLM)

Selective Laser Melting (SLM) is the primary manufacturing method for most critical components in this project. The parts are printed, depowdered, removed from the print bed, and heat-treated by Chinese suppliers. The DfM guidelines for SLM are discussed in a dedicated subsection below.

Material Advantages	Disadvantages	Typical Applications
PLA Very easy to print, good surface finish, affordable, low warping	Not heat-resistant (glass transition $\sim 60^{\circ}\text{C}$ ), brittle at low temperatures, limited mechanical strength	Prototypes, visual models, non-critical covers, cold flow test parts
PETG Durable, flexible, heat/UV/chemical resistant, less brittle than PLA	Slightly harder to print than PLA, prone to stringing, highly absorbent to moisture	General-purpose test bench parts, jigs, functional prototypes
ABS Strong, impact-resistant, better heat resistance ( $\sim 100^{\circ}\text{C}$ ), machinable	Warping, needs heated bed/enclosure, emits fumes, more difficult to print	Test bench parts at extreme temperature, mechanical enclosures, fixtures

Table 3.4: Comparison of FDM plastics

### 3.2.4 Unconventional Machining

#### Electric Discharge Machining (EDM) drilling

Electric discharge machining (EDM) drilling is a non-traditional machining process that uses electrical discharges (sparks) to erode material from a workpiece. Unlike conventional drilling, it does not apply mechanical force, allowing for the creation of very small, high-precision holes while minimizing the risk of drill bit breakage or part damage. This method is especially useful for drilling into hard materials or producing holes with a high depth-to-diameter ratio, where traditional techniques may fail or cause defects.

## 3.3 Expected manufacturing processes

Additive Manufacturing → CNC Machining → EDM Drill → Manual Finishing (Deburring, Tapping, Polishing)

## 3.4 Experimental Validation of Additive Manufacturing

Additive manufacturing is a new and promising method, but its real use for rocket engine parts still needs to be proven. To verify the capabilities, a few small test prints were made. These helped to see which features can be built well, where problems appear (like trapped powder or rough surfaces), and what kind of post-processing might be needed. The results gave useful insight for improving both the design and the choice of manufacturing method.

### BROKE 1

BROKE 1 is the first iteration of the BROKE. It was designed to be a fully functional rocket engine. However, due to time and budget constraints, it was not completed as a fully functional



Figure 3.5: EDM drilling machine in a local machine shop. The machinist was using a magnifier to carefully align the electrode with the small printed holes on the MCC.

rocket engine; only the combustion chamber was printed.

The BROKE 1 MCC was printed in AlSi<sub>10</sub>Mg using Selective-Laser-Melting (SLM) technology. The print has some notable features:

- Wall thickness of 1.5mm
- Cooling channels: 25° helix angle with 1.5mm x 1.5mm smallest cross-section at the throat
- Overhang flange with structurally integrated support
- Flat surfaces for sealing faces

The chamber was printed by a commercial supplier. The build plate orientation and printing direction are shown in Figure 3.6. The print results were as follows:

- No major defects observed. The overall geometry looked fine (Figure 3.6)
- Critical measurable dimensions were within 0.2mm of tolerance
- The overhang flange was successfully printed with integrated support (Figure 3.7)
- Surface finish was acceptable (as-printed roughness around 10-15  $\mu\text{m}$  Ra)
- Cooling channels were **not** fully cleared

While most of the features were printed decently, the cooling channels presented a significant issue. As shown in Figure 3.8, the radial ports were open and allowed water to flow through, but the axial ports were clogged, resulting in little to no flow. This is likely due to the process of SLM printing by the supplier. The general process flow is as follows:

Printing → Depowdering → Heat treatment → Cutting the parts from the bed  
→ Removing support (optional) → Sand/Glass-bead blasting (optional)

The cooling channels were likely to be clogged during the depowdering step. Because the axial ports were located on the build plate, powder may not have been able to fully escape from the channels. In contrast, the radial ports were open to the sides, creating escape paths for the powder. Any powder that remained in the channels was later re-sintered during heat treatment, becoming fully solidified and blocking the channels.

**In conclusion,** BROKE 1 proved that Additive Manufacturing was feasible for MCC. The successful printing of thin walls, overhang features, and cooling channels demonstrated the capability of SLM technology for rocket engine components. However, the experience also highlighted critical limitations, such as powder removal challenges and the risk of channel blockage, which must be addressed in future designs.

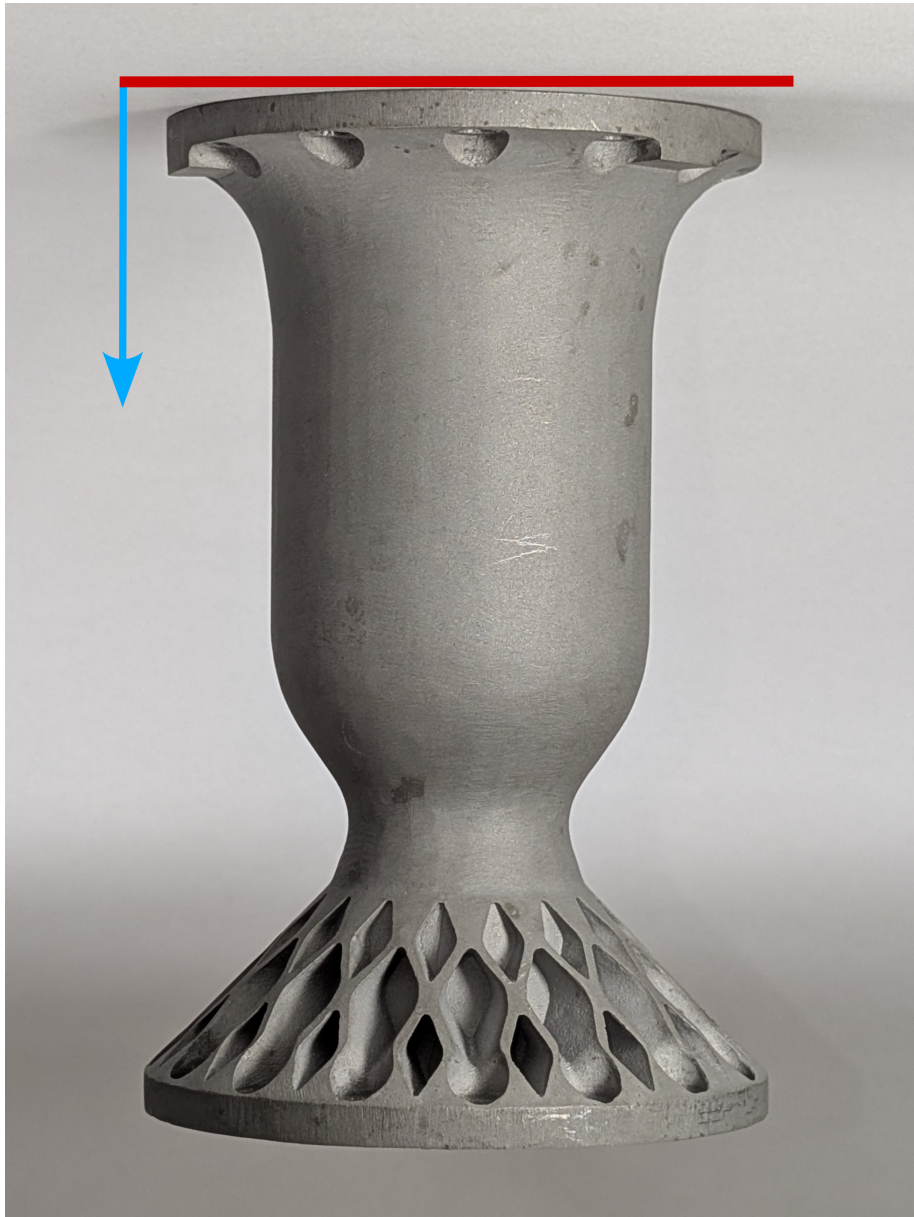


Figure 3.6: BROKE 1 Combustion Chamber  
The red line represents the build plate orientation. The blue arrow indicates the printing direction.



Figure 3.7: The Flange with integrated support



Figure 3.8: Cooling channel ports in a cold flow test

### 3.4.1 BROKE 2 test section

This part's main geometry was derived from the throat section of the main BROKE 2 MCC. The test section was designed to replicate the critical features of the MCC throat, including wall thickness, cooling channel cross-section, and overall contour. By isolating this region, the test print allowed for focused evaluation of manufacturability—specifically, the ability to print thin walls and clear cooling channels without distortion or powder blockage.

The test print was produced using SLM in AlSi<sub>10</sub>Mg, matching the material and process of the full-scale MCC. Key observations included:

- The wall thickness and channel geometry were successfully printed, with dimensional accuracy within 0.15 mm.
- Cooling channels were fully cleared, confirming that the revised orientation and powder escape paths were effective.
- Surface finish was consistent with previous prints, with roughness around 10–15  $\mu\text{m}$  Ra.
- No major distortion or warping was observed, validating the design for thin-walled features.

To derisk the BROKE 2 manufacturing process, a test part was designed. This part was derived from the throat section of the main BROKE 2 MCC, including wall thickness, cooling channels, and overall contour.

Other features of the test print also included (Figure 3.9):

- Injection holes (red arrows): horizontal orientation, 1 mm diameter, dedicated for the injector print
- Printed drilled-size hole for tapping (green circle): for NPT 1/8 thread
- Powder escape arches (blue circle)

The test print was produced using SLM in AlSi<sub>10</sub>Mg, matching the material and process of the full-scale MCC. Key observations included:

- Due to a communication issue, the part was unintentionally ground by the supplier; however, this did not affect its functionality as a test print.
- The overall geometry of the test print looks fine.
- The channels were completely depowdered, and the consistency between channels looks good, except for four ports affected by the injection holes' internal structure, which should not affect the MCC or injector functionalities (see Figure 3.10 for cooling channels cold flow test).
- The injection holes were successfully printed, with a diameter of around 1 mm (see Figure 3.11 for injection holes cold flow test).
- The printed drilled-size hole for tapping was acceptable. The NPT 1/8 thread was successfully tapped. A plastic 3D-printed fitting was able to be fastened in, allowing the part to be attached to a household water tap.

From this test print, it was confirmed that the design for manufacturability guidelines were effective. The successful printing of thin walls, cooling channels, and small features demonstrated the capability of SLM technology for rocket engine components. The experience also provided confidence that the full-scale BROKE 2 MCC could be manufactured successfully using the same design principles.

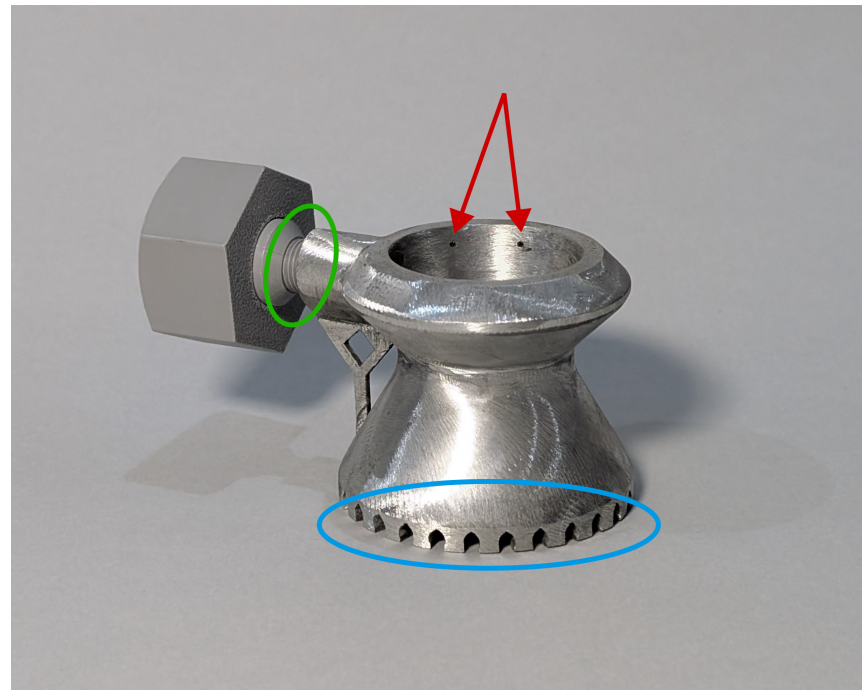


Figure 3.9: BROKE 2 test print with the throat section  
Injection holes in red arrows  
Powder escape arches in the blue circle  
Drilled-size hole for tapping in the green circle

### 3.4. Experimental Validation of Additive Manufacturing



Figure 3.10: Flow test of the cooling channels  
The water can be seen exiting from the exit ports.



Figure 3.11: Flow test of the injection holes  
The water jets from eight injection holes impinged at the center.

### Thrust Frame with supported overhang surface

The thrust frame was not a test part, but a fully functional component. However, because it was inexpensive to print and not a critical part, it was intentionally designed with overhang features that had not been fully derisked at the time. In addition to their functional role, these features provided an opportunity to validate the manufacturability of overhangs in an actual print.

The overhangs in question are the feet of the thrust frame—flat surfaces intended for fastener heads to sit on. For SLM, support structures are always required for such horizontal overhangs. This is because SLM has poor bridging ability: the fine metal powder must be melted, and cannot span gaps like the stringing action in plastic FDM processes. Without support, the overhang surfaces would sag or fail to form properly.

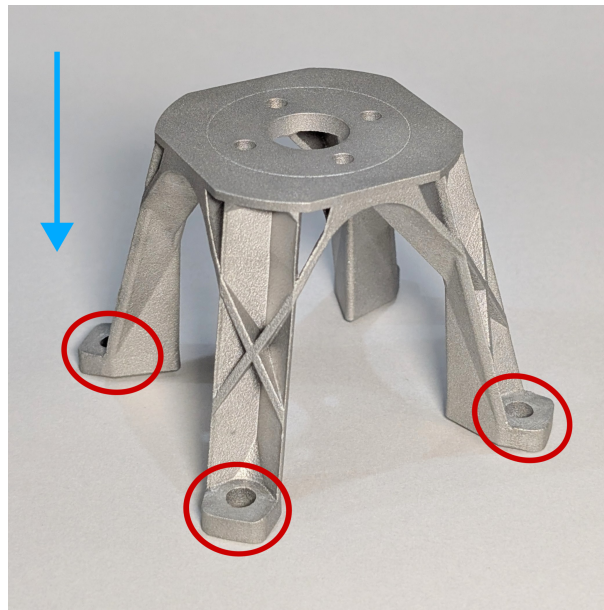


Figure 3.12: Thrust frame  
 The blue axis shows the printing orientation  
 The overhang "foot" features are circled in red.

The printed part clearly showed the overhang's limitation: there was a rough surface left by the support removal process. However, the overall quality was acceptable—the flat surfaces had decent flatness and were suitable for fastener heads.

**This result demonstrated** that overhangs with support structures are manufacturable in SLM, but the support removal process leaves a rough finish. Therefore, while supported overhangs are feasible, this approach is not recommended for critical features that require high surface flatness or tight dimensional tolerances.

## 3.5 SLM Additive Manufacturing Specific DfM

As most components are produced by additive manufacturing, these guidelines are the highest priority for this project. Additive manufacturing enables the creation of complex features that were previously unachievable with traditional methods.

However, as AM is a rapidly evolving field, it is essential to understand and follow empirical and experimental rules developed through recent research and hands-on experience. The recommendations below are based on both literature and practical experience from test prints.

- **Walls and Overhangs**

- Minimum wall thickness can be as low as 0.8 mm, but thicker walls are recommended for rocket engines to reduce erosion risk from rough surfaces and low hardness.
- Overhang angles down to 38° are printable, but angles of 45° or greater are preferred for better surface finish and to minimize support requirements.
- Support structures are suitable for non-critical external features. Modern suppliers can reliably remove supports, and post-processing methods such as glass blasting produce smooth, high-quality surfaces.

- **Holes and Threads**

- *Horizontally-oriented holes:*

- \* The maximum recommended diameter is 6 mm (absolute maximum 8 mm). For larger holes, use diamond or teardrop profiles. For threaded holes, end-milling may be needed before tapping.
    - \* Minimum diameter is 1 mm.

- *Horizontally-oriented threads:*

- \* For thread sizes below M8, direct tapping is suitable. Print the hole 0.1 mm smaller than the tap drill size.
    - \* For M8 and larger, enlarge the printed hole to the tap drill size with an end-mill before tapping to improve thread quality and reduce tap breakage risk.

- *Vertically-oriented holes:* Use holes larger than 1.0 × 1.0 mm.

- *Vertically-oriented threads:* Print the hole 0.1 mm smaller than the tap drill size; direct hand tapping is suitable.

- Thread engagement depth should be at least 1.0 times the thread diameter.

- **Cooling Channels**

- Minimum cooling channel cross-section is 1.0 × 1.0 mm, with a preferred aspect ratio of 1:1 (square) for optimal perimeter-to-area ratio.
- Helix angles of 25° are feasible; smaller angles are likely possible, but larger angles may be problematic.
- Design channels with direct escape paths for powder removal, especially for those with ports on the build plate.

- **Surface Finish**

As-printed surface finish is generally acceptable, but for critical sealing surfaces, post-processing (milling or turning) with high-quality finishing passes is required.

#### Design Validation Methods

In order to perform a Design Rule Check (DRC) on SLM printed CAD models, it is recommended to first use common FDM slicer software (e.g., Cura, PrusaSlicer, or OrcaSlicer) to digitally identify any manufacturability issues, such as unsupported overhangs, thin walls, or problematic features. The slicer provides a fast, visual way to catch potential problems before fabrication.

Optionally—but highly recommended if an FDM printer is available—the models can then be physically printed using FDM. While SLM requires much stricter design guidelines than FDM, plastic printing remains a valuable validation process, especially considering the massive cost difference between metal SLM printing and plastic FDM printing. Physical prints allow for hands-on inspection of critical features, tolerances, and assembly fit. This step is extremely cost-effective and provides practical feedback, helping to refine the design and ensure all features are suitable for additive manufacturing before committing to expensive metal prints.

Beyond these guidelines, additive manufacturing offers significant design freedom, limited only by imagination and process constraints.

## 3.6 Lessons learned

**Chinese SLM Printing Suppliers** To reduce supply-chain risks, the parts were printed by two separate selective laser melting (SLM) suppliers in China. Both suppliers delivered good quality parts at an affordable cost. Surface finishing services, such as glass-bead blasting, were very helpful in improving surface smoothness and making support removal easier. Both suppliers also offered heat treatment at no extra cost, but the process quality was not verified under this project scope.

#### Machining Procedure for Surface Finish

Face milling should be performed last to maintain "mirror" surface finish, especially on sealing surfaces. If other machining operations (e.g., end milling, drilling, tapping) are performed after face milling, they may leave tool marks or scratches on the sealing surface. These imperfections can compromise the seal integrity and require additional polishing or re-machining to restore the surface quality. By scheduling face milling as the final machining step, the sealing surfaces remain pristine and ready for assembly without further finishing work.

#### Vertical Integration

Because of limited resources, most manufacturing processes were outsourced to several local machine shops, each with its own technical specialization. This setup sometimes caused inconsistencies in part quality, slower communication, and difficulties in coordinating the manufacturing sequence. For example, EDM drilling and CNC machining were performed at different facilities. This separation created extra logistical challenges, such as transporting parts between shops, matching production schedules, and maintaining consistent quality standards. To reduce these issues, future projects should aim for greater vertical integration—either by developing in-house manufacturing capability or by working with a single, full-service machine shop.

# Chapter 4

## Main Combustion Chamber (MCC)

### 4.1 Material Selection

The main criteria for MCC material selections are: strength at elevated temperature, thermal properties, manufacturability, and cost. As discussed in section 3, due to local availability and cost, only stainless steel 316L and aluminum AlSi<sub>10</sub>Mg are considered as the candidates for MCC material. However, we will try to keep the discussion as general as possible.

Property	Stainless Steel 316L	AlSi <sub>10</sub> Mg
Yield Strength (MPa) @ 200°C	360–390 [1]	158 Mpa [2]
Max Operating Temperature	650°C	300°C
Thermal Conductivity (W/mK)	16.3	130
Density (g/cm <sup>3</sup> )	8.00	2.67
Machinability	Good, but needs special tools	Excellent, easy to machine

Table 4.1: Comparison of MCC material candidates: mechanical, thermal, and manufacturing properties.

For this project, the chamber pressure  $P_c$  of 20 bar is modest, and any decent metallic alloy should be able to handle this pressure with appropriate wall thickness—provided the material can be kept at a safe operating temperature. This shifts the focus from pure mechanical strength to thermal management and the material’s ability to facilitate effective cooling.

As established in the system architecture (Chapter 2), regenerative cooling is the primary thermal management strategy for this engine, making thermal conductivity a critical material property. The effectiveness of regenerative cooling directly determines whether materials with lower high-temperature strength can be successfully employed.

**AlSi<sub>10</sub>Mg** has relatively low strength at elevated temperatures and begins to weaken significantly around 300°C. However, its exceptional thermal conductivity—about 10 times greater than stainless steel 316L—makes it highly effective at transferring heat from the hot gas side to the cooling channels. This property is crucial for maintaining low wall temperatures and preventing thermal failure. In essence, aluminum's viability depends entirely on the cooling system's effectiveness, and its high thermal conductivity is a major asset in achieving this goal.

**Inconel and Titanium alloys**, while maintaining excellent strength even at elevated temperatures, suffer from poor thermal conductivity (similar to stainless steel). Their superior mechanical properties are not necessary for the modest chamber pressures in this engine, and their poor thermal performance would actually hinder the regenerative cooling strategy. Additionally, these materials are expensive and difficult to machine.

**Stainless Steel 316L** offers a middle ground with moderate strength at elevated temperatures, but it shares the same fundamental limitation as high-strength alloys: poor thermal conductivity that impedes heat transfer to the cooling fluids.

**Copper alloys** (i.e. GrCop) would be the technically optimal choice, combining the highest thermal conductivity of all metals with good strength retention at high temperatures. However, they are prohibitively expensive and extremely difficult to machine, making them impractical for this project.

**The final decision**, AlSi<sub>10</sub>Mg was selected as the optimal compromise: it is affordable, easily machinable, and has excellent thermal conductivity that supports the regenerative cooling strategy. Its use requires careful cooling system design to maintain safe wall temperatures, but this aligns with the project's primary technical challenge of developing an effective regenerative cooling system. While it is not a primary concern for this student project, the lightweight nature of aluminum is an additional bonus.

## 4.2 de Laval Nozzle Contour Profiling

### 4.2.1 Geometry Study with a Simplified Conical Nozzle

This section demonstrates how hand calculations can be performed for a simplified conical nozzle, using key empirical design coefficients to guide the process. While detailed numerical results are not provided, the focus is on illustrating the methodology and how these parameters shape the chamber and nozzle geometry.

The designing steps for a simplified conical nozzle are as follows (with required geometrical parameters:  $D_c$  – cylindrical section diameter,  $L_c$  – combustion and contraction length,  $D_t$  – throat diameter,  $\beta$  – convergent half-angle,  $\alpha$  – divergent half-angle,  $L_e$  – exit length,  $D_e$  – exit diameter)

- Define the design parameters: chamber pressure ( $P_c$ ), exit pressure ( $P_a$ ), bulk mass flow rate ( $\dot{m}$ ), and propellants and their O/F mixture ratio.
- Run NASA CEA analysis for Rocket analysis to get thermodynamics properties, in the case of cylindrical chamber design, especially the *Coefficient of thrust  $C_F$* , *Characteristic velocity*

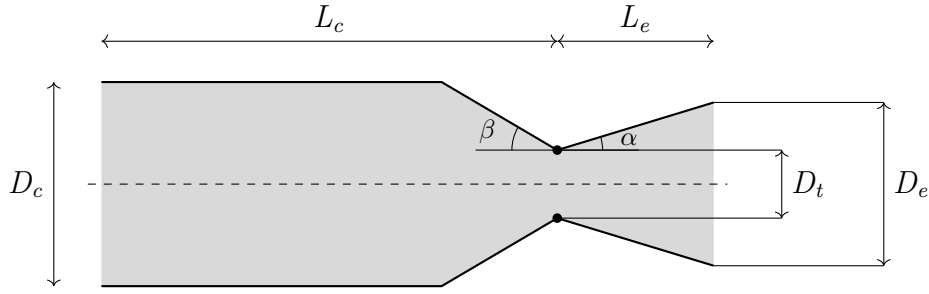


Figure 4.1: Cross-section of a simplified conical nozzle showing key design parameters: chamber diameter ( $D_c$ ), throat diameter ( $D_t$ ), exit diameter ( $D_e$ ), chamber length ( $L_c$ ), exit length ( $L_e$ ), convergent half-angle ( $\beta$ ), and divergent half-angle ( $\alpha$ ).

$c^*$ , and *Specific impulse*  $I_{sp}$ .

- Get the throat diameter  $D_t$

$$A_t = \frac{F_t}{(P_c)_{ns} \times C_f}$$

**Note:** The throat diameter is the decisive parameter in nozzle design due to the thermodynamics of compressible flow. For ideal gases, it is directly determined by chamber pressure, temperature, and gas properties through choked flow conditions. For real gas mixtures with complex chemistry, the throat area is typically determined experimentally, as it depends on the specific thermochemical properties with parameters **characteristics velocity**  $c^*$  of the combustion products.

- For **cylindrical chamber section**

- Find the chamber diameter  $D_c$  with the throat diameter  $D_t$  and contraction ratio  $\frac{D_c}{D_t}$
- Estimate the cylindrical chamber length  $L_{chamber}$  based on experimental results

- For **the contraction section** of the nozzle

- Design a conical convergent profile from chamber diameter  $D_c$  to throat diameter  $D_t$  using half-angle  $\beta$  and length  $L_c$

- For **the expansion section** of the nozzle

- Calculate the optimal expansion ratio  $\epsilon = A_e/A_t$  with isentropic flow relations
- Find the nozzle exit diameter  $D_e$  with the optimal expansion ratio  $\epsilon$
- Estimate the nozzle length  $L_n$  with the half-angle  $\alpha$

- Plot the contour profile with the calculated parameters

### 4.2.2 Empirical design parameter study

#### Cylindrical chamber section: Contraction ratio $A_c/A_t$

The contraction ratio  $A_c/A_t$  is the ratio of the chamber cross-sectional area  $A_c$  to the throat area  $A_t$ . This parameter is crucial for minimizing pressure losses and ensuring combustion efficiency and stability within the chamber.

According to Sutton [3]<sup>1</sup>, a contraction ratio above 2.0 results in only a 0.55% loss of specific impulse ( $I_{sp}$ ), while a ratio of 3.5 reduces the loss to 0.31%. Hutzel and Huang[4] (Figure 1-10) show that total pressure loss is minimal for contraction ratios above 3. For  $A_c/A_t = 2$ , the Mach number in the cylindrical chamber is about 0.32 for combustion products with  $\gamma = 1.2$ .

If the contraction ratio is too small, the flow accelerates rapidly in the cylindrical section immediately after the injector (Rayleigh flow), resulting in high-speed flow near the injector. This can reduce combustion efficiency, compromise flame stability, and make ignition more difficult.

In practice, a contraction ratio above 3 is generally sufficient for stable combustion and minimal pressure loss. Beyond this threshold, the ratio is determined by practical constraints such as engine packaging, injector size, cooling channel manifolds, and manufacturability. The chamber diameter should be large enough to accommodate these features, but not excessively large to avoid unnecessary weight and volume.

For this design, after several iterations, a final **contraction ratio of  $A_c/A_t = 4.885$**  was selected, resulting in a chamber diameter  $D_c$  of 50 mm.

#### Cylindrical chamber section: $L^*$ characteristic length

$L^*$  is widely used in rocket engine design to characterize the combustion chamber size relative to the throat area. It determines the residence time of the propellants in the chamber, which affects combustion efficiency and completeness. The  $L^*$  parameter is defined as:

$$L^* = \frac{V_c}{A_t} \quad (4.1)$$

$V_c$  is the volume of the combustion chamber

$A_t$  is the throat area

While  $L^*$  is not a strictly critical parameter, its main role is to ensure sufficient combustion time. The typical  $L^*$  values found in Sutton or Hutzel and Huang are based on empirical results from larger engines. For small-scale engines like this one, the optimal  $L^*$  may differ.

To reference  $L^*$  at a similar engine scale, NASA Technical Note D-126 by Samuel (1959) [5] is used. This paper describes the development of a 250-pound thrust rocket engine and provides published  $L^*$  experimental results.

"Tests on similar engines with variations in the combustion-chamber length revealed that there was no appreciable increase in performance at 600 pounds per square inch chamber pressure for engines having a characteristic length greater than 14 [inches]."  
— NASA Technical Note D-126, Stein (1959)

Based on this, an  **$L^*$  of 350 mm ( $\approx 14.76$  in)** is selected as a minimal threshold for this design. After several design iterations, it was extended to 375 mm to accommodate the cooling channel manifolds and provide a better sealing surface for the nozzle assembly. This results in a total chamber length of 135 mm, which is a reasonable size for manufacturability and integration.

---

<sup>1</sup>Rocket Propulsion Elements (7th Edition, Table 3-2)

	<b>BROKE 2</b>	<b>NASA D-126</b>
Thrust (N)	1000	$\approx 1111.3$
Chamber Pressure (bar)	21	$\approx 41.4$
Propellants	LOX/Ethanol	LOX/JP-4
Injector Type	Swirl Coaxial	High-density Shear Coaxial

Table 4.2: Comparison of BROKE 2 and NASA D-126 engine

**Convergent section: Contraction half-angle  $\beta$** 

According to Hutzel and Huang, a convergent half-angle ( $\beta$ ) between  $20^\circ$  and  $45^\circ$  is typical for rocket nozzles. A smaller angle reduces the risk of flow separation and improves performance, but increases the overall length and weight of the nozzle. Conversely, a larger angle shortens the nozzle, but can increase the risk of flow separation and pressure losses.

From a design-for-manufacturability (DfM) perspective, the half-angle  $\beta$  should not exceed  $45^\circ$ , as larger angles may result in unsupported overhangs or poor surface finish, depending on the build orientation and manufacturing process.

In summary, the selected convergent half-angle is  $\beta = 30^\circ$ .

**Divergent section: Expansion half-angle  $\alpha$** 

For conical nozzles, Sutton recommends a divergent half-angle ( $\alpha$ ) of  $15^\circ$ , which has become the unofficial standard for comparing correction factors, energy losses, and nozzle lengths:

A half-angle value of  $15^\circ$  has become the unofficial standard of reference for comparing correction factors or energy losses, or lengths from different diverging conical nozzle contours.

— Rocket Propulsion Elements, 9th Edition, Sutton (2016)

As with the convergent section, DfM considerations dictate that the half-angle  $\alpha$  should not exceed  $45^\circ$  to avoid unsupported overhangs or poor surface finish, depending on build orientation.

It should be noted, however, that in this design the divergent half-angle  $\alpha$  is ultimately unused, as the nozzle contour is generated as a bell-shaped profile using computer code rather than a simple conical geometry.

**Divergent section: Optimal expansion ratio  $\epsilon$** 

The expansion is optimized at 0.7 atm ambient conditions.

### 4.2.3 Summarization of MCC design points and the main internal contour

The following table summarizes the main design points of the MCC:

Parameters	Value
$\dot{m}$	0.5 kg/s
Oxidizer	O <sub>2</sub> (L)
Fuel	C <sub>2</sub> H <sub>5</sub> OH(L)
$O/F$	1.5
$P_e$	0.8 atm
$A_c/A_t$	4.88513
Nozzle shape	80% length bell nozzle
$L^*$	0.375 m
Convergence half angle $\beta$	30°

Table 4.3: Main Desgin Parameters

From those design points, the main internal contour of the MCC can be generated using RPA (Rocket Propulsion Analysis) software. The following figure shows the contour of the MCC.

#### 4.2. de Laval Nozzle Contour Profiling

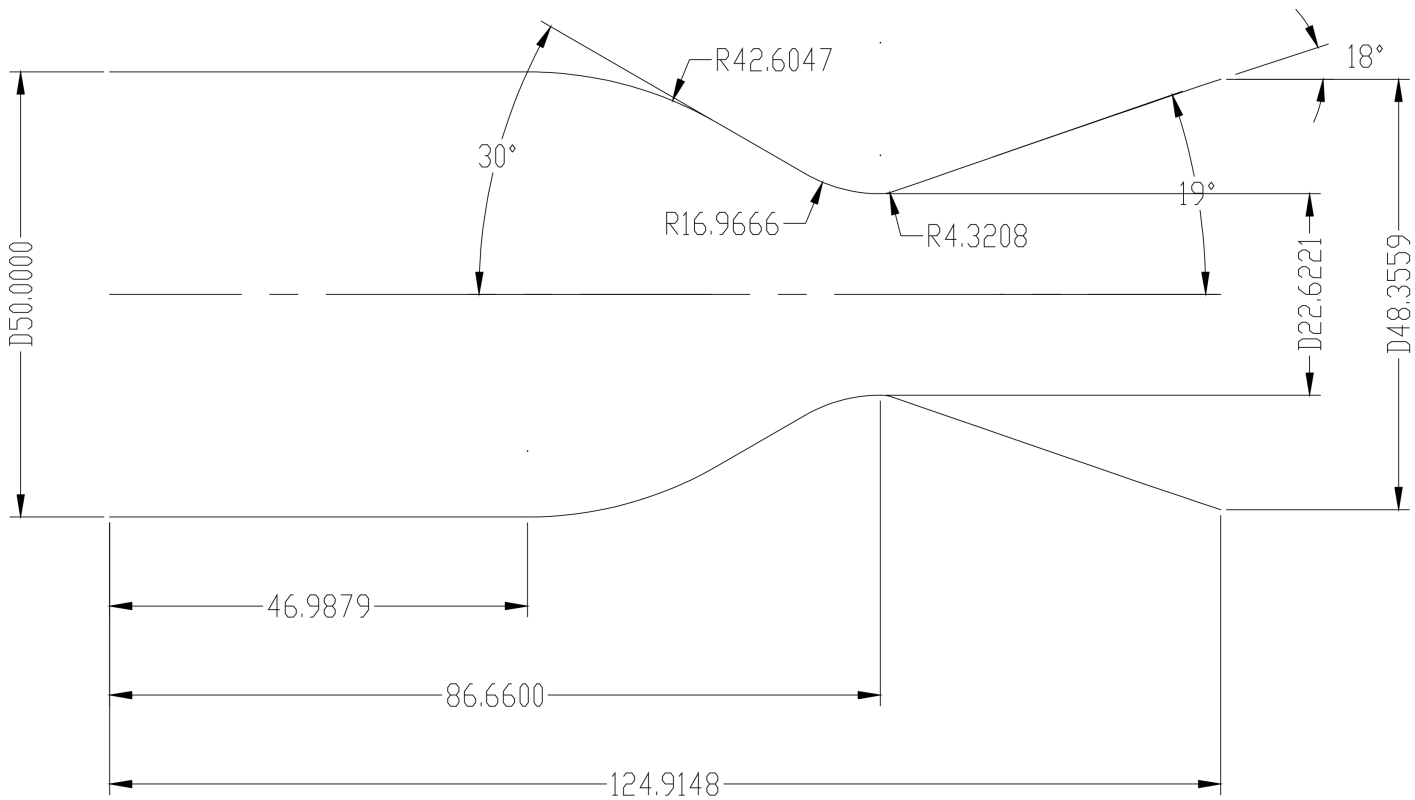


Figure 4.2: BROKE 2 MCC Contour with  $L^*$  set to 350 mm as a minimum threshold. The cylindrical section length was later extended to accommodate the cooling channel manifolds and provide a better sealing surface for the nozzle assembly.

## 4.3 Regenerative cooling circuit analysis

### 4.3.1 Introduction

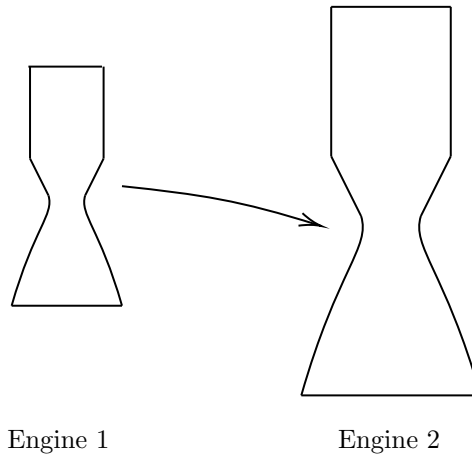
#### What is Regenerative Cooling?

Regenerative Cooling is the use of propellants as coolant to absorb heat from the combustion chamber and nozzle walls before being injected into the combustion chamber. This method effectively manages the extreme thermal loads experienced during rocket engine operation, preventing structural failure due to overheating. By circulating the propellant through cooling channels embedded in the chamber walls, regenerative cooling not only protects the engine components but also preheats the propellant, enhancing combustion efficiency.

### 4.3.2 Challenges

#### Square-cube problem

The square-cube problem is a fundamental geometric principle that describes how an object's volume and surface area scale with size. As linear dimensions increase by a factor  $L$ , volume scales as  $L^3$  while surface area scales as  $L^2$ . This scaling relationship creates significant challenges for thermal management in rocket engines, particularly for regenerative cooling systems.



In rocket engines, thrust is proportional to the mass flow rate of propellant, which scales with combustion volume ( $\propto L^3$ ). However, regenerative cooling only needs to manage heat transfer through the chamber wall surface, not remove all heat generated in the combustion volume. The cooling system creates a thermal boundary layer that insulates the wall from hot combustion gases. As engine size increases, thrust increases cubically while the available cooling surface area increases only quadratically, creating a more favorable thrust/cooling-surface ratio for larger engines.

This scaling advantage is dramatically illustrated by the Saturn V F-1 engine, where "only" 70% of the fuel flow was diverted for regenerative cooling of the thrust chamber, with the remaining 30% admitted directly to the main injector manifold [6]. Despite the cooling requirement for a massive engine, the F-1's large scale made regenerative cooling feasible.

Conversely, small-scale engines face an increasingly unfavorable thrust/cooling-surface ratio, making effective thermal management one of the primary technical challenges in small rocket engine design. This fundamental scaling constraint drives the critical importance of the regenerative cooling system design for the BROKE 2 engine.

Square-cube problem also affects the manufacturability of the cooling system. For example, film cooling requires a certain minimum hole diameter to be reliably drilled, which may not be feasible for small engines. For example, a common target film cooling mass flow rate is 5% of the total propellant flow. For a small engine with a total mass flow rate of 0.5 kg/s, this corresponds to only 0.025 kg/s of coolant, while a large engine with a mass flow rate of 10kg/s is 0.5 kg/s of coolant. Assuming the same coolant density and velocity, the small engine would require a cooling hole area 20 times smaller than the large engine. If the large engine requires 10 holes of 1 mm diameter, the small engine would need holes of only 0.22 mm diameter, which may be impractical to manufacture reliably. Similarly, cooling channels must be large enough to allow sufficient coolant flow without risking clogging due to additive manufacturing limitations. These practical manufacturing constraints further complicate the design of effective regenerative cooling systems for small rocket engines.

### Balancing Surface Area and Flow Velocity

Conventional cooling systems, such as air coolers, dissipate heat to ambient air (an effectively infinite thermal reservoir). In these systems, surface area and flow velocity can be optimized independently: surface area is maximized through fin arrays, while flow velocity is increased using fans or pumps.



Figure 4.3: An air cooler with dense fin array for maximizing surface area, and dual fans for high flow velocity

Courtesy of Rascom Computerdistribution Ges.m.b.H.

Rocket engines impose a fundamentally different constraint: the coolant mass flow rate is fixed by overall engine design and performance requirements. To establish the theoretical foundation, this analysis initially assumes **isotropic heat flux**, where chamber wall temperature is uniform and heat flux is constant around the channel perimeter (Figure 4.4):

For cooling channels, the heat transfer rate from the wall to the cooling fluid is governed by Newton's law of cooling:

$$\dot{Q} = \int P \cdot h \cdot \Delta T dz \quad (4.2)$$

$\dot{Q}$  is the heat transfer rate

$h$  is the convective heat transfer coefficient

$P$  is the wetted perimeter of the channel

$\Delta T$  is the temperature difference between the wall and the fluid

$z$  is the length along the centerline of the engine (Figure 4.5)

The convective heat transfer coefficient  $h$  is a function of the coolant flow velocity  $v$ . Assuming turbulent flow in the cooling channels and the temperature differences are large,  $h$  can be estimated

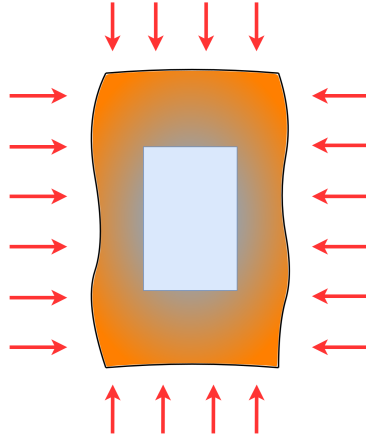


Figure 4.4: Simplified cooling channel with isotropic heat flux

using the *Sieder-Tate correlation*:

$$h = 0.027 \cdot \frac{k}{D_h} \cdot Re^{0.8} \cdot Pr^{1/3} \cdot \left( \frac{\mu}{\mu_w} \right)^{0.14} \quad (4.3)$$

$k$  is the thermal conductivity of the fluid

$D_h$  is the hydraulic diameter

$Re$  is the Reynolds number

$Pr$  is the Prandtl number

$\mu$  is the dynamic viscosity at bulk fluid temperature

$\mu_w$  is the dynamic viscosity at wall temperature

The Reynolds number  $Re$  is defined as:

$$Re = \frac{\rho \cdot v \cdot D}{\mu} \quad (4.4)$$

$\rho$  is the fluid density

$\mu$  is the dynamic viscosity of the fluid

The bulk flow velocity  $v$  is related to the mass flow rate  $\dot{m}$  as:

$$v = \frac{\dot{m}}{\rho \cdot A_c} \quad (4.5)$$

$A_c$  is the cross-sectional area of the channel

$\rho$  is the fluid density

$\dot{m}$  is the mass flow rate of the fluid

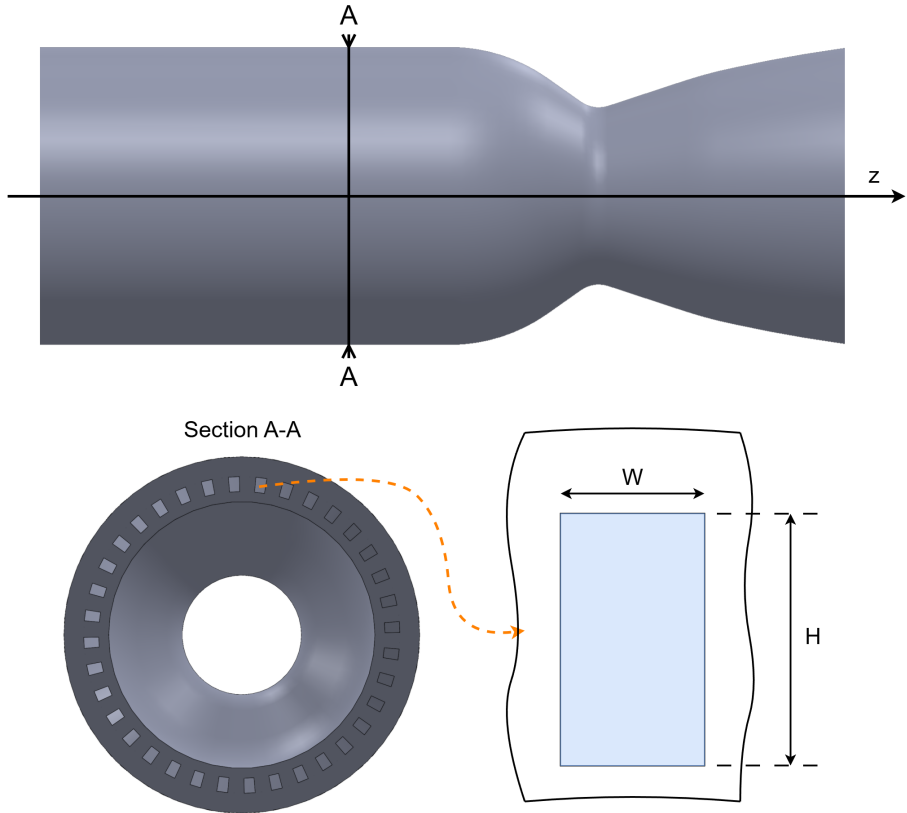


Figure 4.5: The dimensions of the rocket engine with a cross-section cut

The hydraulic diameter  $D_h$  is defined as:

$$D_h = \frac{4 \cdot A_c}{P} \quad (4.6)$$

$A_c$  is the cross-sectional area of the channel

$P$  is the wetted perimeter of the channel

Substituting equations 4.3, 4.4, 4.5, and 4.6 into equation 4.2 and performing algebraic manipulation yields the fundamental heat transfer relationship:

$$\dot{Q} = C \int P \cdot v^{0.8} \cdot A_c^{-0.8} \cdot \left( \frac{\mu}{\mu_w} \right)^{0.14} \cdot \Delta T dz \quad (4.7)$$

where  $C = 0.027 \cdot k \cdot \left( \frac{\rho}{\mu} \right)^{0.8} \cdot \dot{m}^{0.8} \cdot Pr^{1/3}$  contains all fluid properties and mass flow rate.

**Square Channel Analysis:** For square channels with side length  $s$ , the geometric relationships are  $A_c = s^2$  and  $P = 4s = 4\sqrt{A_c}$ . Substituting into equation 4.7:

$$\dot{Q} = C \int 4\sqrt{A_c} \cdot \left( \frac{\dot{m}}{\rho \cdot A_c} \right)^{0.8} \cdot A_c^{-0.8} \cdot \left( \frac{\mu}{\mu_w} \right)^{0.14} \cdot \Delta T dz = C \int 4A_c^{-0.3} \cdot \left( \frac{\mu}{\mu_w} \right)^{0.14} \cdot \Delta T dz \quad (4.8)$$

This reveals a fundamental trade-off: increasing cross-sectional area  $A_c$  increases surface area as  $P \propto \sqrt{A_c}$  but simultaneously decreases flow velocity as  $v \propto A_c^{-1}$ . The net effect is  $\dot{Q} \propto A_c^{-0.3}$ , indicates that larger square channels provide **worse heat transfer** due to the stronger influence of reduced velocity compared to the surface area benefit.

This counterintuitive result demonstrates that simply enlarging channels is not an effective cooling strategy—the velocity penalty outweighs the surface area advantage. However, increasing the flow velocity has a caveat: it increases the pressure drop across the cooling circuit. This limitation will be discussed in more detail in the **AM and System Constraints** 4.3.2 section.

### High Aspect Ratio Cooling Channels (HARCC)

High aspect ratio rectangular channels decouple surface area from flow velocity, enabling independent optimization of these competing parameters. For rectangular channels with width  $w$ , height  $h$ , and aspect ratio  $AR = \frac{h}{w}$ , the geometric relationships are:

$$w = \sqrt{\frac{A_c}{AR}} \quad (4.9)$$

$$h = \sqrt{A_c \cdot AR} \quad (4.10)$$

$$P = 2\sqrt{A_c}(1 + \sqrt{AR}) \quad (4.11)$$

Substituting into the heat transfer equation yields:

$$\dot{Q} = C \int 2(1 + \sqrt{AR}) \cdot A_c^{-0.3} \cdot \left( \frac{\mu}{\mu_w} \right)^{0.14} \cdot \Delta T dz \quad (4.12)$$

High aspect ratio channels increase the perimeter factor  $(1 + \sqrt{AR})$  without changing the cross-sectional area  $A_c$ , maintaining constant flow velocity while enhancing heat transfer surface area. For example, increasing  $AR$  from 1 to 9 doubles the factor  $(1 + \sqrt{AR})$  from 2 to 4, resulting in a 100% improvement in heat transfer rate for the same cross-sectional area.

However, the effectiveness of HARCC is fundamentally limited by **fin efficiency**, as the thin walls between channels function as cooling fins. The fin efficiency depends on the fin geometry and the material's thermal conductivity. **HARCC is particularly beneficial for chambers made of high thermal conductivity materials such as copper and aluminum**, where the excellent thermal conductivity maintains high fin efficiency and maximizes the benefit of increased perimeter. For low thermal conductivity materials (e.g., Inconel), fin efficiency is reduced, and the advantages of HARCC are limited.

Additionally, the previous analysis assumed isotropic heat flux, but in rocket engines, heat transfer occurs primarily from the hot gas side (Figure 4.6), further emphasizing the importance of fin efficiency in the channel design.

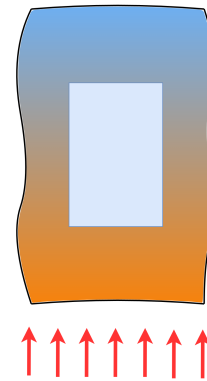


Figure 4.6: Rocket engine cooling channel with one hot-side heat source

HARCC provides multiple advantages: low pressure drop, maintained high flow velocity, increased surface area for heat transfer, and improved fin efficiency for high thermal conductivity materials, making it advantageous for regenerative cooling in small rocket engines.



Figure 4.7: Vulcain 2 chamber with slotted milled cooling channels. Courtesy of WELT [7]

However, while high aspect ratio cooling channels offer significant theoretical advantages, their practical implementation is constrained by additive manufacturing limitations, as discussed in the following section **AM and System Constraints 4.3.2**.

#### **System and Additive manufacturing AM Constraints**

From system-level requirements, we prefer the cooling channels to have as low pressure drop as

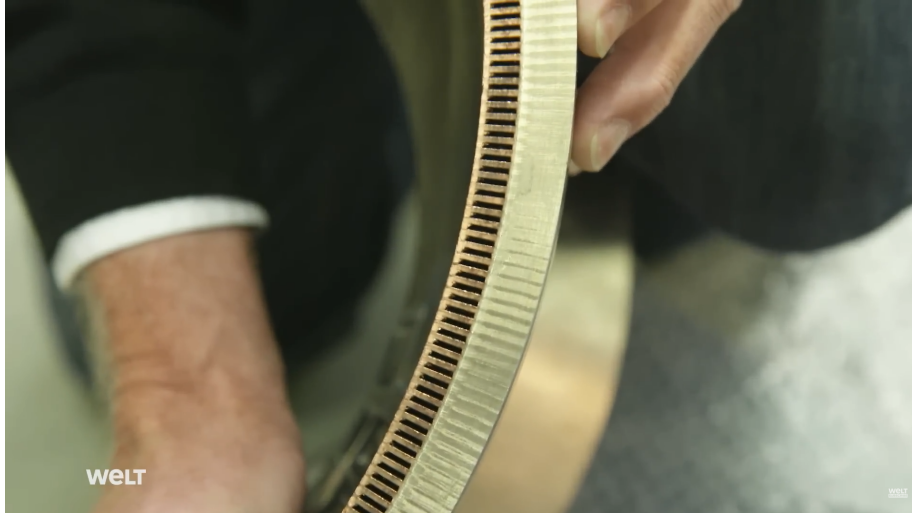


Figure 4.8: Vulcain 2 cooling channels cross-section. Courtesy of WELT [7]

possible, to minimize the stress on the pressure-fed system. However, we also learned from the previous section **Balancing Surface Area and Flow velocity** 4.3.2 that high flow velocity is beneficial for heat transfer. Therefore, a balance must be struck between minimizing pressure drop and maximizing flow velocity to achieve effective cooling performance.

As already mentioned in chapter 3, the main AM constraints for the cooling channels are:

- Minimum feature size: The smallest channel dimension that can be reliably printed is 1.0x1.0mm
- Aspect ratio: In the case of very small channels, the aspect ratio should be close to 1:1 to reduce the area/perimeter ratio for depowdering.

These constraints limit the achievable aspect ratio and minimum channel size, impacting the design of high aspect ratio cooling channels. For example, while a very high aspect ratio (e.g., 10:1) may be theoretically optimal for heat transfer, practical AM limitations may restrict the aspect ratio to a maximum of 5:1 or even 3:1, depending on the specific manufacturing process and material. Due to the low TRL of AM, a conservative approach is taken to ensure manufacturability and reliability. We prefer to go with low aspect ratio channels (e.g., 3:1 or 2:1) to ensure successful printing and depowdering, even if it means sacrificing some theoretical heat transfer performance.

### Conclusions of challenges

- The square-cube problem creates a fundamental scaling challenge for regenerative cooling in small rocket engines, as thrust scales with volume ( $\propto L^3$ ) while cooling surface area scales with area ( $\propto L^2$ ). This makes effective thermal management increasingly difficult at smaller scales, especially with the lack of coolant (one of the propellants).
- Simply enlarging cooling channels does not solve the problem, as it reduces flow velocity and convective heat transfer, leading to worse overall cooling performance. In fact, we might

prefer flow velocity over surface area.

→ However, flow velocity can not be increased too high due to pressure drop

- High aspect ratio rectangular channels can break the area-velocity trade-off by increasing perimeter (and thus surface area) without changing cross-sectional area. This allows simultaneous maximization of surface area and maintenance of high flow velocity, significantly improving heat transfer rates.  
→ However, the practical implementation of high aspect ratio channels is constrained by additive manufacturing limitations, such as minimum feature size and aspect ratio restrictions. These constraints must be carefully balanced against the theoretical benefits to achieve an effective regenerative cooling design.

### Cooling circuit system-level requirements

: Descending in terms of priority, the main system-level requirements for the cooling circuit are:

- Cool the engines effectively to prevent thermal failure
- Manufacturability
- Minimize pressure drop to reduce stress on the pressure-fed system
- Even temperature distribution to reduce thermal stress and maximize the cooling efficiency (no hotspots or no coldspots)

The boundary conditions for designing the cooling circuit

Coolant: Ethanol Chamber material: AlSi<sub>10</sub>Mg, thermal conductivity: 120 W/m-K, and target max wall temperature: 300°C

### 4.3.3 BROKE 2 Regenerative Cooling Circuit Features

Since channels cannot be made too small or employ high aspect ratios, alternative approaches are required. Fortunately, additive manufacturing (AM) enables complex geometries not possible with traditional methods. Therefore, several design strategies can be explored to enhance cooling performance without relying solely on channel size or aspect ratio.

#### Double pass cooling circuit

Due to additive manufacturing (AM) limitations, it is not feasible to produce highly dense, small cooling channels. To overcome this and still achieve high coolant velocity for effective heat transfer, a double-pass cooling circuit is implemented in BROKE 2.

At the design point, with a throat diameter of 22.62 mm, 1 mm × 1 mm channels, and a coolant mass flow rate of 0.2 kg/s ( $\approx 2.535 \times 10^{-4}$  m<sup>3</sup>/s), the required number of channels for a coolant velocity of 18 m/s (as a representative example for calculation) is:

$$\begin{aligned} N_{\text{channels}} &= \frac{\dot{V}}{A \cdot v} \\ &= \frac{2.535 \cdot 10^{-4} \text{ m}^3/\text{s}}{1 \cdot 10^{-6} \text{ m}^2 \times 18 \text{ m/s}} \\ &\approx 14 \text{ channels} \end{aligned}$$

where  $\dot{V}$  is volumetric flow rate,  $A$  is channel cross-sectional area, and  $v$  is coolant velocity.

With only 14 channels with the size of  $1 \text{ mm} \times 1 \text{ mm}$ , the wetted perimeter at the throat is just 19.7% of the total ( $\pi D_t \approx 71.0 \text{ mm}$ ), leaving much of the wall insufficiently cooled and prone to hotspots (see Figure 4.9, which illustrates the concept using a generic engine geometry).

The double pass circuit (Figure 4.10) uses red arrows for the first pass (inlet flow) and blue arrows for the second pass (return flow), enabling higher coolant velocities and improved heat transfer even within AM constraints. This approach is especially beneficial for small-scale engines, where maximizing cooling efficiency is critical for safe operation and material durability.

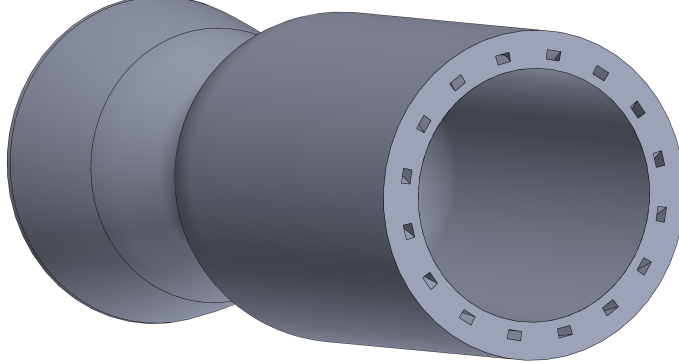


Figure 4.9: Single-pass regenerative chamber at the designed flow velocity.  
The channels are too sparse to provide effective cooling.

### Helical channels

Additive manufacturing (AM) imposes a strict lower limit on the minimum printable feature size, typically around 1 mm. This constraint can limit the ability to optimize cooling channel geometry for maximum heat transfer, since smaller channels generally improve cooling performance but may be unprintable. Helical channels offer a practical solution to this limitation: by wrapping the channel in a helix around the chamber wall, the effective channel length and the surface area are both increased, extending the contact duration between coolant and hot wall.

Importantly, this geometric approach does not require reducing the channel cross-section below the AM threshold, so there is no penalty on flow velocity due to a smaller channel size. In fact, as illustrated in Figure 4.11, the helical configuration can increase the effective flow velocity for a given mass flow rate, since the projected channel width along the chamber axis is reduced by the helix angle  $\alpha$ :

$$W_{\text{eff}} = W_{AM} \cdot \cos \alpha$$

This reduction in *hydraulic cross-sectional area*<sup>2</sup> increases the flow velocity, which further enhances convective heat transfer. Thus, helical channels simultaneously maximize surface area, contact time, and flow velocity—overcoming the typical trade-offs discussed in Section 4.3.2—and enable higher cooling performance within the constraints of AM.

---

<sup>2</sup>the cross-section perpendicular to flow's vector

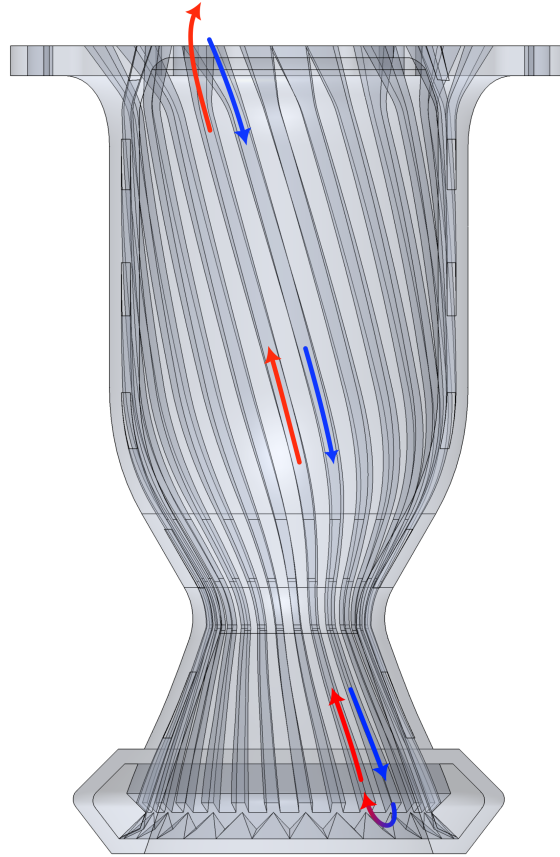


Figure 4.10: Double pass cooling flow path.  
Red arrows indicate the first pass – inlet; blue arrows show the second pass – return.

The increase in cooling channel length can also be calculated as:

$$L_{\text{cooling channels}} = \frac{L_{\text{chamber}}}{\cos \alpha}$$

For this project, a helix angle of  $\alpha = 25^\circ$  was selected as a balance between maximizing effective channel length and maintaining manufacturability. This moderate angle provides a 10% increase in both surface area and flow velocity without creating overly tight helices that could complicate printing or depowdering.

#### **Variable cross-sectional cooling channels**

From Sutton<sup>3</sup>

For many liquid propellant rockets, coolant velocities in the chamber vary from approximately 3 to 10 m/sec or 10 to 33 ft/sec, and at the nozzle throat from 6 to 24 m/sec or 20 to 80 ft/sec

---

<sup>3</sup>Sutton, Rocket Propulsion Elements (9th ed.) page 296

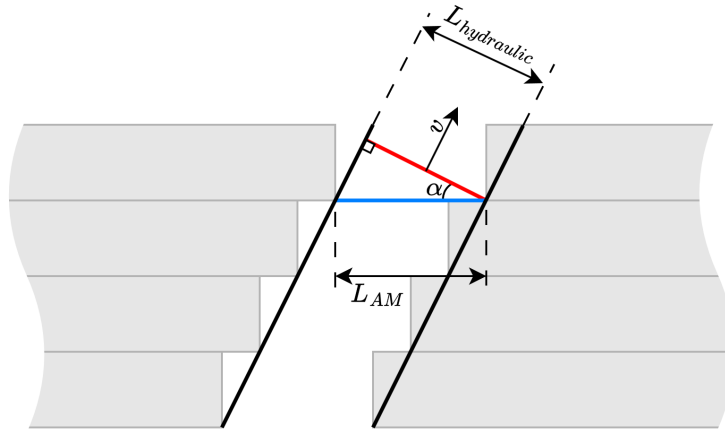


Figure 4.11: Helical channel illustration

Later on, in *Loosely-Coupled Method 4.3.4*, we will learn that the heat flux is three times higher at the throat than in the cylindrical section. Therefore, it is logical to design the flow velocity at the throat to be approximately three times higher than in the cylindrical section or nozzle extension.

If one wishes to do a detailed design study, the *Loosely-Coupled Method 4.3.4* explained below can be used to optimize the channel cross-section along the chamber length to maintain a target flow velocity profile that matches the local heat flux by

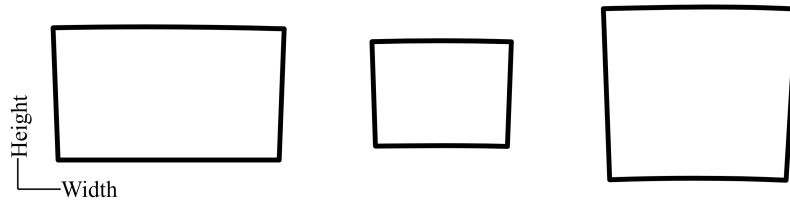
- Set the wall temperature at a desired value (e.g. 200°C)
- Find the heat flux at each section along the chamber length using RPA
- Calculate the required coolant side convective heat transfer coefficient  $h$  at each section
- Calculate the required flow velocity  $v$  at each section using Sieder-Tate correlation
- Calculate the required channel cross-section  $A_c$  at each section using the mass flow rate equation

However, for simplicity and manufacturability, we approximate the variable cross-section cooling channels using three discrete sections: cylindrical, throat, and nozzle. The channel dimensions are selected to achieve a flow velocity ratio of approximately 1:3:1.17—where the nozzle section velocity is set slightly higher than the cylindrical section, mainly due to manifold layout constraints, not strictly the velocity ratio. The resulting channel dimensions and aspect ratios, chosen to balance cooling performance and manufacturability, are summarized in Figure 4.12.

### Film cooling

Film cooling is a technique where a small portion of the coolant is intentionally injected through holes in the chamber wall to create a thin protective layer (or "film") of coolant between the hot combustion gases and the chamber wall. This film acts as a thermal barrier, reducing the convective heat transfer from the hot gases to the wall and thereby lowering the wall temperature.

There are two main design considerations for film cooling:



	Cylindrical	Throat	Nozzle
Height	1.5 mm	1.0 mm	2.0 mm
Width	2.5 mm	1.2 mm	2.2 mm
Area	$3.75 \text{ mm}^2$	$1.2 \text{ mm}^2$	$4.4 \text{ mm}^2$
Aspect Ratio	0.60	0.83	0.91

Figure 4.12: Variable cross-section cooling channel illustration and corresponding channel dimensions.

- **Location of film cooling ports:** The film cooling holes can be located at the injector (top of the engine), which is the case for most engines, or at the start of the throat section (e.g. RD-191), or at the expansion nozzle (e.g. F-1)
- **Geometry of film cooling ports:** The geometry of the film cooling holes can vary, with common designs including simple round holes, shaped holes (e.g. slots or elliptical holes), or even complex geometries like angled or curved holes to optimize the coolant flow and coverage.

In this project, film cooling accounts for 5% of the total propellant mass flow. The film cooling system consists of 14 holes, each with a diameter of 0.3 mm, which are compatible with local manufacturing capabilities while ensuring even distribution. These holes are positioned at the start of the throat section, located 1.35 mm from the chamber wall. This proximity ensures that the film cooling layer can effectively protect the wall from the hot combustion gases, reducing the local heat flux and helping to maintain safe wall temperatures. The distribution of the film cooling ports is illustrated in Figure 4.13.

### Summary

In summary, the BROKE 2 cooling circuit uses a combination of double-pass flow, helical channels, variable cross-sections, and film cooling to overcome additive manufacturing constraints. These features maximize the wetted perimeter, contact time, and flow velocity, resulting in more effective and reliable cooling, even with practical limits on channel size and aspect ratio. This integrated approach leverages the advantages of additive manufacturing to enable safe operation and material durability for small-scale rocket engines.

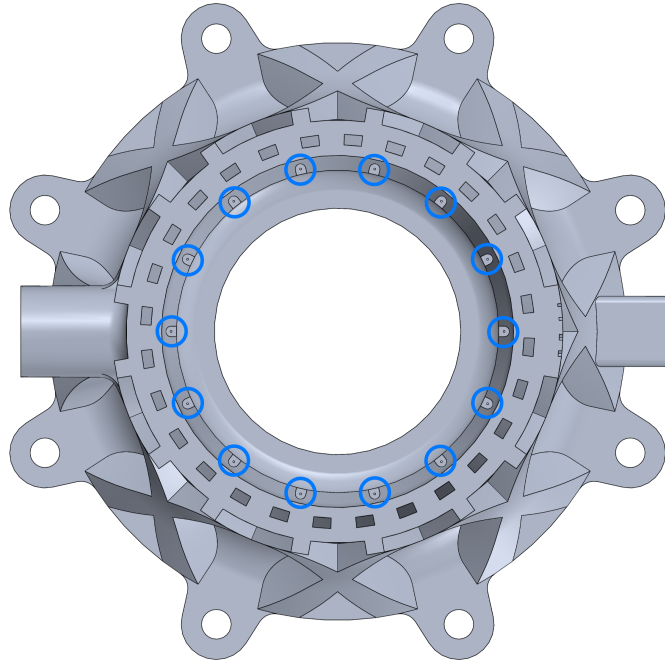


Figure 4.13: Film cooling ports' distribution, in MCC cross-sectional cut  
The tiny film cooling ports are circled in blue

#### 4.3.4 Analysis methods

##### One-dimensional Analysis

Before jumping into complex analyses, we have to understand the heat transfer phenomenon at the rocket engine wall by simplifying the heat transfer process in one dimension. We assume the heat transferred to the environment is negligible, and the engine is adiabatic, which is a reasonable assumption for a regeneratively cooled engine. The heat transfer schematic is shown in Figure 4.14.

The heat flux transferred through the engine is

$$\begin{aligned}\dot{q} &= (T_{gas} - T_{coolant}) \div \Sigma R_{thermal} \\ &= (T_{gas} - T_{coolant}) \div \frac{1}{h_h} + \frac{t_{wall}}{k_{wall}} + \frac{1}{h_c}\end{aligned}$$

Where:

- $T_{gas}$  is the temperature of the hot gas.
- $T_{coolant}$  is the temperature of the coolant
- $h_h$  is the convective heat transfer coefficient of the hot gas
- $h_c$  is the convective heat transfer coefficient of the coolant

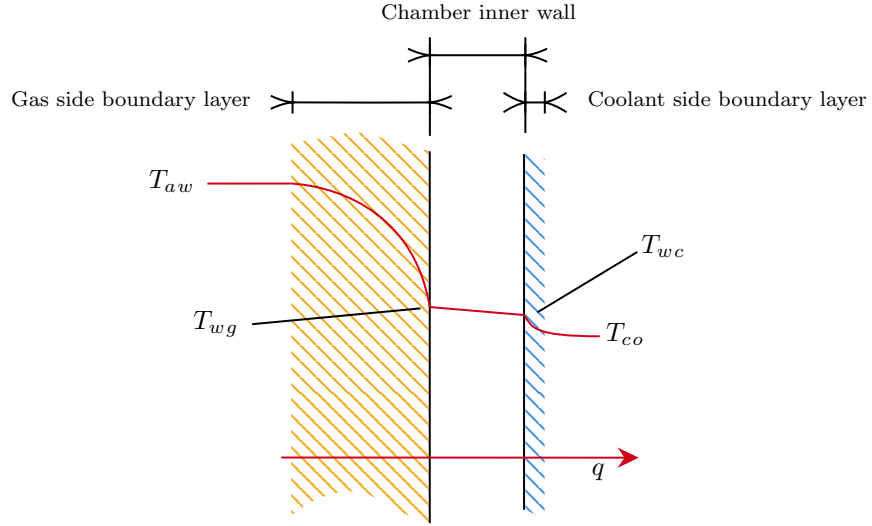


Figure 4.14: Heat transfer schematic

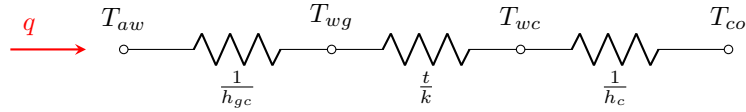


Figure 4.15: Thermal Resistance Circuit

- $k_{wall}$  is the thermal conductivity of the wall material
- $t_{wall}$  is the wall thickness

The wall thermal conduction is trivial. However, in the case of fluid-solid boundary, finding the convection heat transfer coefficient is another story.

Coolant side convection heat transfer coefficient can be assumed to be calculated using:

- Sieder-Tate equation: in the case of subcooled liquid cooling
- Nucleate boiling: in case of nucleate boiling, the  $h_c$  does not need to be calculated. From Incropera (p. 658), during nucleate boiling, the  $T_{wc}$  is fixed between  $T_{sat}$  and  $T_{sat} + 30^\circ\text{C}$ . Therefore, the heat transfer coefficient can be calculated as:

The hot-side convection heat transfer coefficient can be derived from Bartz correlation. The gas-side boundary layer: Bartz correlation

$$h_g = 0.026 \left( \frac{G^{0.8} c_p^{0.6} \mu^{0.2}}{D_t^{0.2} r_t^{0.1} Pr^{0.6}} \right) \left( \frac{T_{aw}}{T_{wg}} \right)^{0.68} \quad (4.13)$$

where:

- $h_g$  : Hot-gas side heat transfer coefficient ( $\text{W}/\text{m}^2\text{K}$ )
- $G$  : Mass flux at the throat ( $\dot{m}/A_t$ ),  $\text{kg}/(\text{m}^2\text{s})$
- $c_p$  : Specific heat at constant pressure ( $\text{J}/\text{kg K}$ )
- $\mu$  : Dynamic viscosity ( $\text{kg}/\text{m s}$ )
- $D_t$  : Throat diameter (m)
- $r_t$  : Throat radius of curvature (m)
- $Pr$  : Prandtl number
- $T_{aw}$  : Adiabatic wall temperature (K)
- $T_{wg}$  : Wall temperature (K)

### Loosely-coupled Method

The analysis of regenerative cooling in rocket engines is complicated by the fact that the Bartz correlation requires both the adiabatic wall temperature ( $T_{aw}$ ) and the actual wall temperature ( $T_{wg}$ ), neither of which is known at the outset of the design process. The inclusion of film cooling further increases the complexity of the calculation. As a result, an iterative approach is typically required to converge on a solution for both heat flux and wall temperature. This iterative process, where both heat flux and wall temperature are solved simultaneously until convergence, is referred to in this thesis as the *tightly-coupled method*.

In practice, FEA/CFD programs can accurately solve conduction and subcooled liquid convection heat transfer, and their results can later be coupled into thermal-mechanical solvers. However, they cannot directly solve the hot-side convection heat transfer due to the lack of suitable empirical correlations. Conversely, Rocket Propulsion Analysis (RPA) can estimate hot-side convection using empirical methods, but it cannot accurately model conduction and subcooled liquid convection heat transfer.

Therefore, a compromise is needed. Due to local resource constraints—limited computational power and time—the loosely-coupled method is chosen for this project as a practical, rapid-iteration approach. While integrating the Bartz correlation directly into FEA/CFD software would enable fully-coupled thermal analysis, this is not currently feasible. For future projects requiring higher numerical accuracy, scripting dynamic boundary conditions (such as the Bartz correlation for hot-gas heat transfer) in Ansys via Python will be considered.

One common method in research is to use Rocket Propulsion Analysis (RPA) for designing regenerative cooling circuits. However, based on the author's experience, RPA has notable drawbacks for this application:

- RPA cannot converge solutions for double-pass regenerative circuits with film cooling.
- RPA is limited to one-dimensional analysis. While this may be sufficient for the hot gas side, it cannot accurately capture the complex geometry of the coolant side (e.g., channels with ribs or fins), leading to potential inaccuracies.

These limitations motivate the need for a more flexible approach. By decoupling the hot-side and coolant-side convection heat transfer, we arrive at the *loosely-coupled method*.

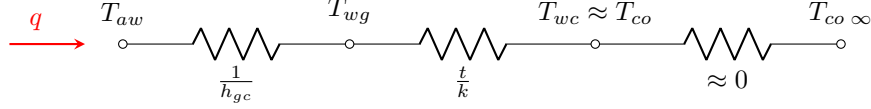


Figure 4.16: Loosely Coupled Thermal Resistance Circuit, with reservoir assumption and its temperature of  $T_\infty$

Simply speaking, instead of solving both the hot-side and coolant-side convection heat transfer simultaneously, we first solve the hot-side convection heat transfer using RPA, assuming an idealized cooling reservoir. This reservoir fixes the wall temperature at a value limited by the material's operating limit. With this assumption, we can determine the heat flux and hot-gas wall temperature. These values are then used to evaluate the coolant-side performance separately. The overall heat transfer schematic is shown in Figure 4.16.

The ***loosely-coupled method*** can be summarized in the following steps:

1. **Assume an Ideal Cooling Reservoir:** Substitute the real coolant (e.g., fuel) with an ideal cooling reservoir, assuming negligible coolant-side thermal resistance. This simplifies the analysis and sets a constant wall temperature. The heat transfer schematic is shown in Figure 4.17.

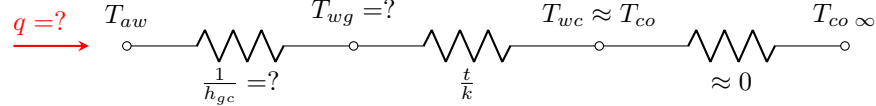


Figure 4.17: Loosely Coupled Thermal Resistance Circuit with reservoir assumption  
The Unknowns: heat flux  $q$ , hot-gas wall convection heat transfer coefficient  $h_{gc}$ , and wall temperature  $T_{wg}$ .

2. **Calculate Hot-side Convection:** Analyze the hot-side wall convection heat transfer using RPA, as shown in Figure 4.18. RPA provides the heat flux  $q_{\text{evaluate}}$ , hot-gas wall temperature  $T_{wg\text{-baseline}}$ , and hot-gas side convection heat transfer coefficient  $h_{gc}$ .

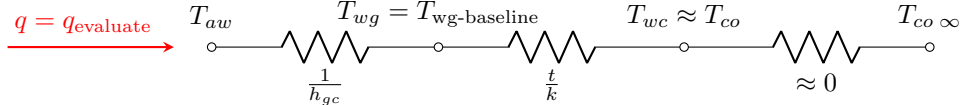


Figure 4.18: Loosely Coupled Thermal Resistance Circuit, analysis with RPA to find  $q$ ,  $T_{wg}$ , and  $\frac{1}{h_{gc}}$ .

3. **Evaluate Cooling Performance:** Use the heat flux from RPA to evaluate cooling performance with the real coolant properties, as shown in Figure 4.19.

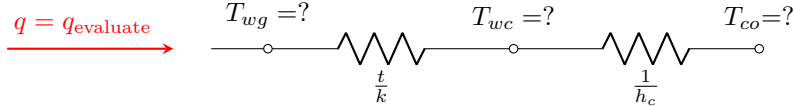


Figure 4.19: Loosely Coupled Thermal Resistance Circuit, heat-flux  $q$  and hot-gas wall temperature  $T_{wg}$  baseline for evaluation.

The ***overall iteration process*** of the ***loosely-coupled method*** is illustrated in Figure 4.20. This approach allows for rapid evaluation of cooling performance while accommodating complex coolant-side geometries and properties, making it well-suited for the design of regenerative cooling.

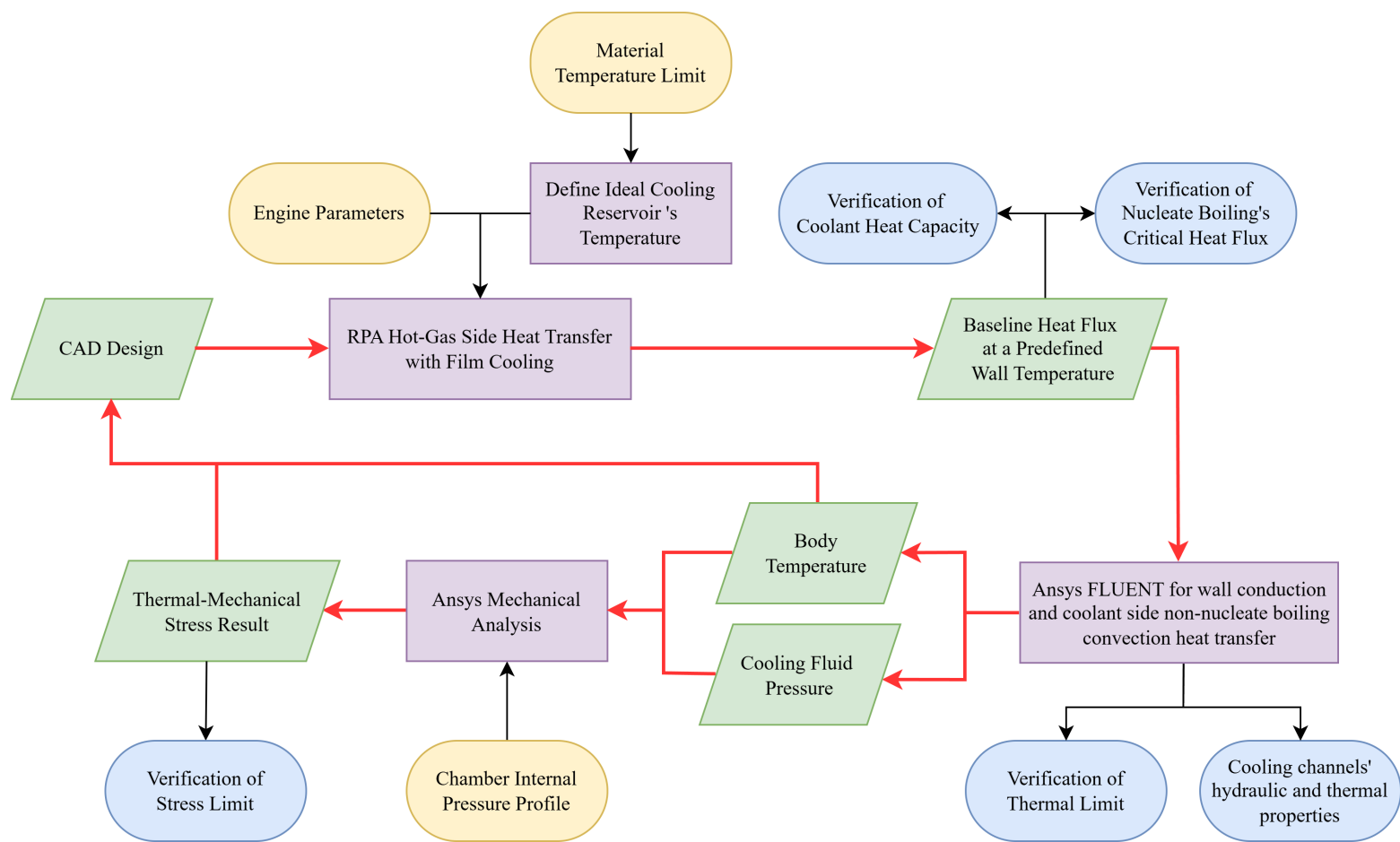


Figure 4.20: Analysis Iteration Process. Red lines indicate main iteration loop

### 4.3.5 Cooling analysis results

#### Coolant Heat Capacity analysis

The coolant used in BROKE 2 is Ethanol, and the pressure at the injector feed pressure is  $P_c = 28 \text{ bar}$ . Thermodynamic properties were evaluated using CoolProp [8]. From the calculations, at 28 bar, the boiling point of Ethanol is 469.95K or 196.8°C. Therefore, we have to ensure that the coolant does not reach this temperature. This can be done by calculating the maximum heat flux that the coolant can handle before reaching its boiling point.

The maximum heat flux that the coolant can handle is given by:

$$q_{\max} = \int_{T_{\text{inlet}}}^{T_{\text{saturation}}} \dot{m} c_p dT \quad (4.14)$$

Where:

$q_{\max}$  : the maximum heat flux that the coolant can absorb before boiling

$T_{\text{inlet}}$  : the inlet temperature of the coolant

$T_{\text{saturation}}$  : the saturation temperature of the coolant at the given pressure

$\dot{m}$  : the mass flow rate of the coolant

$c_p(T)$  : the specific heat capacity of the coolant at pressure

From the figure 4.21 and 4.22, we can see that the specific heat capacity of Ethanol varies significantly with pressure, and is negligibly constant with pressure. This is due to the incompressibility of sub-cooled liquid. Therefore:

$$q_{\max} = \int_{T_{\text{inlet}}}^{T_{\text{saturation}}} \dot{m} c_p(T) dT \quad (4.15)$$

with  $c_p(T)$  is a function of temperature only.

To compute this numerically, we can approximate the integral using discrete temperature steps:

$$q_{\max} \approx \sum_{i=0}^{n-1} \dot{m} \cdot c_p(T_i) \cdot \Delta T \quad (4.16)$$

where  $T_i = T_{\text{inlet}} + i\Delta T$ , and  $\Delta T = \frac{T_{\text{saturation}} - T_{\text{inlet}}}{n}$  with  $n$  being the number of temperature intervals used in the calculation.

From the iteration, the result of the maximum specific heat absorbed:

$$q_{sp} \approx 570 \text{ kJ/kg}$$

For a mass flow rate of  $\dot{m} = 0.2 \text{ kg/s}$ , the maximum heat flux that the coolant can handle is:

$$\dot{q}_{\max} = \dot{m} \cdot q_{sp} = 0.2 \cdot 570000 = 114000 \text{ W} = 114 \text{ kW}$$

Now, assume that the wall temperature is 200°C, we can apply loosely-coupled analysis with the ideal cooling reservoir at  $T_{CO \infty} = 195^\circ\text{C}$ . By doing that, we set the hot-gas wall side temperature to  $\approx 200^\circ\text{C}$ . In this case, the heat flux distribution is the figure 4.23

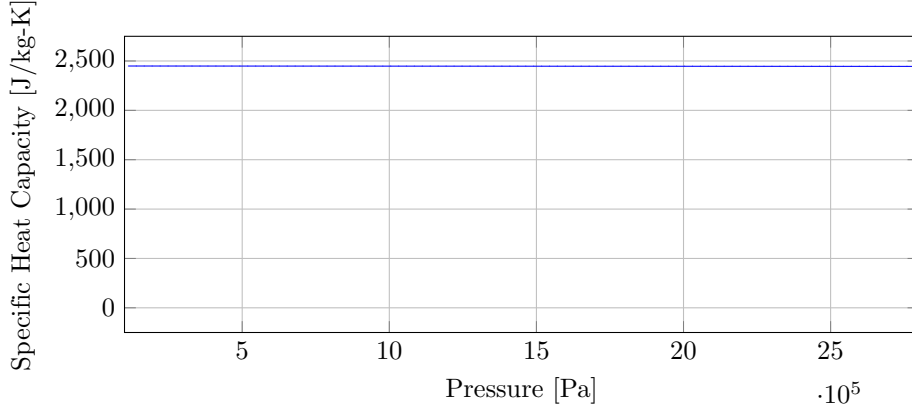


Figure 4.21: Ethanol's Heat Capacity vs Pressure, at T=300 K

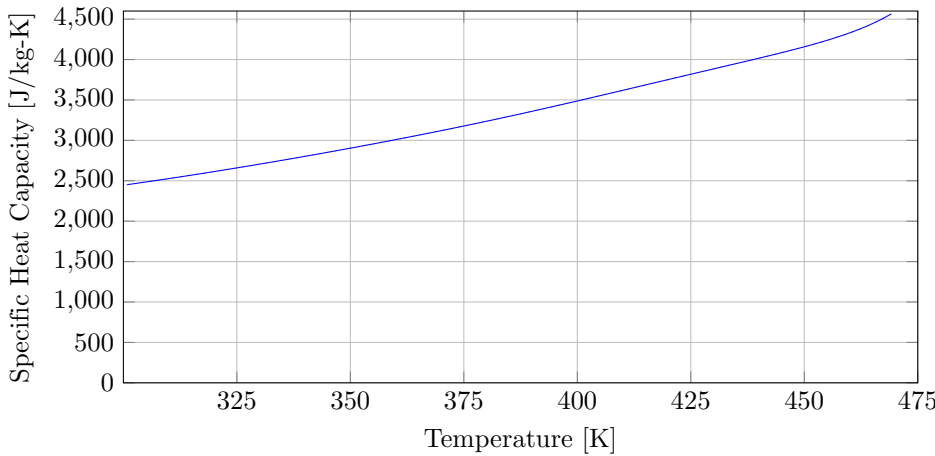


Figure 4.22: Ethanol's Heat Capacity vs Temperature, at P=21 bar

To find the required heat flux to be removed, we integrate:

$$Q = \int \dot{q} dA \quad (4.17)$$

$$= \int_0^L \dot{q} \cdot R \cdot \pi dz \quad (4.18)$$

$$\approx \sum_{i=0}^{n-1} \dot{q} \cdot R \cdot \pi \cdot \Delta z \quad (4.19)$$

where  $R$  is the radius of the chamber, and  $L$  is the length of the chamber. By integrating the heat flux, we can find the total heat flux that needs to be removed by the coolant:  $Q_{\text{required}} = 36.69 \text{ kW}$ .

This value is well below the maximum heat flux that the coolant can handle, which is 114 kW. Therefore, the coolant is enough to cool the engine.

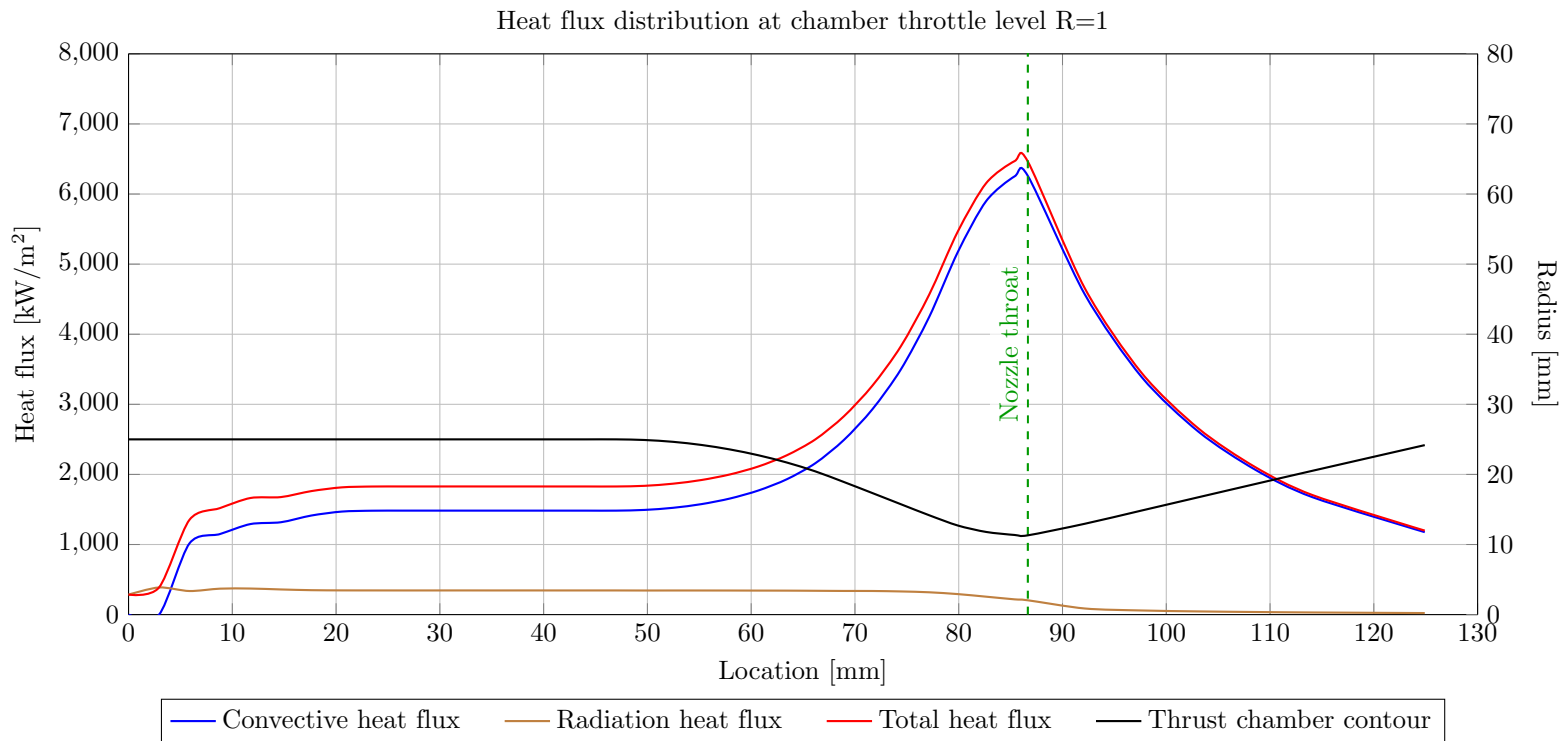


Figure 4.23: Heat Flux with the ideal cooling reservoir at  $T_{CO\infty} = 196^\circ\text{C}$  and  $T_{wg} \approx 200^\circ\text{C}$

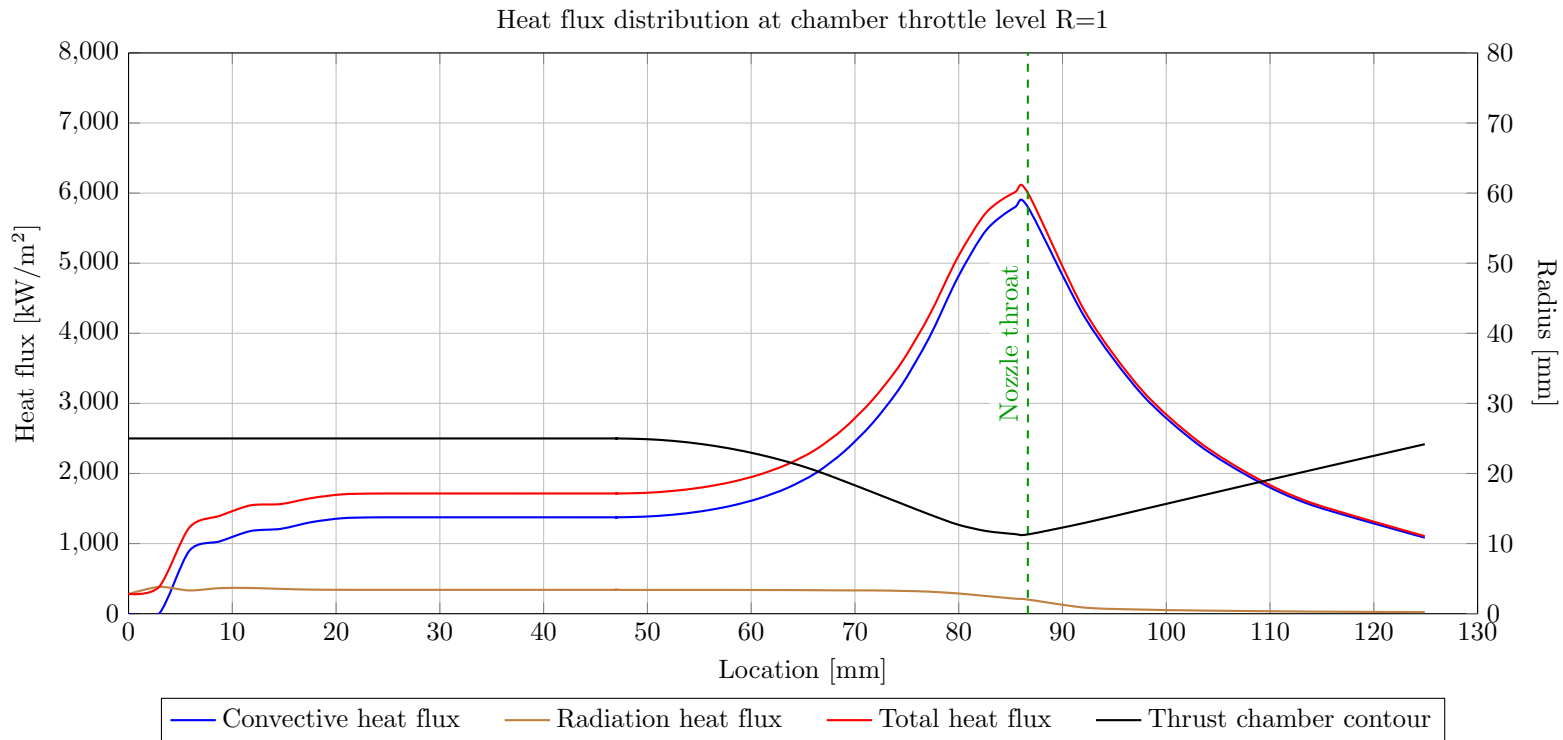


Figure 4.24: Heat Flux with the ideal cooling reservoir at  $T_{CO \infty} = 245^\circ\text{C}$  and  $T_{wg} \approx 250^\circ\text{C}$

### Critical Heat Flux Analysis for Ethanol Coolant

From Incropera<sup>4</sup>, nucleate boiling exists in the range  $(T_{\text{wall}} - T_{\text{saturation}}) < 30 \text{ K}$ , meaning the coolant-side wall temperature is effectively "locked" at up to 30 K above the saturation temperature of ethanol. At 20 bar, the boiling temperature of ethanol is about 183°C (to be checked), so the coolant-side wall temperature will be locked between 183°C and 213°C. This temperature is well below the threshold for 50% strength loss in AlSi<sub>10</sub>Mg, providing a substantial safety margin for engine cooling.

The maximum heat flux is expected when  $\Delta T$  is at its highest, and with  $T_{aw}$  assumed to be constant, coolant temperature  $T_{co}$  is at its lowest temperature. Hence, we can perform loosely-coupled analysis with the ideal cooling reservoir at  $T_{CO \infty} = 200^\circ\text{C}$ . That value is selected as it's above the  $T_{CO \infty}$  for 18K. The heat flux obtained from RPA is then compared to the critical heat flux (CHF) to ensure that the cooling design is within safe limits.

While CHF occurs when localized coolant at the wall reaches the saturation temperature  $T_{\text{sat}}$ , the bulk coolant temperature can be lower than  $T_{\text{sat}}$ —this is known as subcooled boiling. Due to localized boiling in the boundary layer, these fluid elements can reach saturation and trigger CHF, which increases the effective convective heat transfer capacity up to a point.

However, if the imposed heat flux exceeds the critical heat flux, a vapor film rapidly forms on the wall, drastically reducing the heat transfer coefficient. This leads to an abrupt drop in heat flux and a sharp rise in wall temperature, potentially causing thermal failure. Therefore, it is essential to ensure that the design heat flux remains below the CHF threshold to maintain safe and effective cooling performance.

From 4.23, the maximum heat flux when the hot-gas wall temperature  $T_{wg} \approx 200^\circ\text{C}$  is  $\approx 6.5 \text{ MW/m}^2$  or  $\approx 3.97 \text{ BTU}/(\text{in}^2 \cdot \text{s})$ . From Meyer and Linne [9]<sup>6</sup>,  $3.97 \text{ BTU}/(\text{in}^2 \cdot \text{s})$  should be on par with the experimental CHF value.

In conclusion, the chamber heat flux value should be within the nucleate boiling region of Ethanol, which helps with maintaining hot-gas wall temperature at around 200°C, providing a good safety margin for the AlSi<sub>10</sub>Mg chamber.

$$T_{wg \text{ nucleate boiling}} \in [183^\circ\text{C}, 213^\circ\text{C}]$$

### CFD-Based Convection Heat Transfer Analysis

To validate the loosely-coupled method, a convection heat transfer analysis was performed using CFD software (e.g., Ansys Fluent or CFX). The boundary conditions for the simulation are as follows:

- Heat flux: obtained from RPA with an ideal cooling reservoir at  $T_{CO \infty} = 516.15 \text{ K}$  ( $243^\circ\text{C}$ ), and  $T_{wg, \text{ baseline}} \approx 250^\circ\text{C}$
- Coolant: Ethanol
- Coolant mass flow rate  $\dot{m}$ :  $0.2 \text{ kg/s}$
- Coolant inlet temperature  $T_{co, \text{ inlet}}$ :  $20^\circ\text{C}$
- Coolant inlet pressure  $P_{co}$ :  $28 \text{ bar}$

<sup>4</sup>Incropera, Fundamentals of Heat and Mass Transfer (7th ed.), page 658

<sup>5</sup>[https://en.wikipedia.org/wiki/Nucleate\\_boiling#/media/File:Boiling\\_Curve.jpg](https://en.wikipedia.org/wiki/Nucleate_boiling#/media/File:Boiling_Curve.jpg)

<sup>6</sup>Can be downloaded by <https://ntrs.nasa.gov/api/citations/19980017166/downloads/19980017166.pdf>

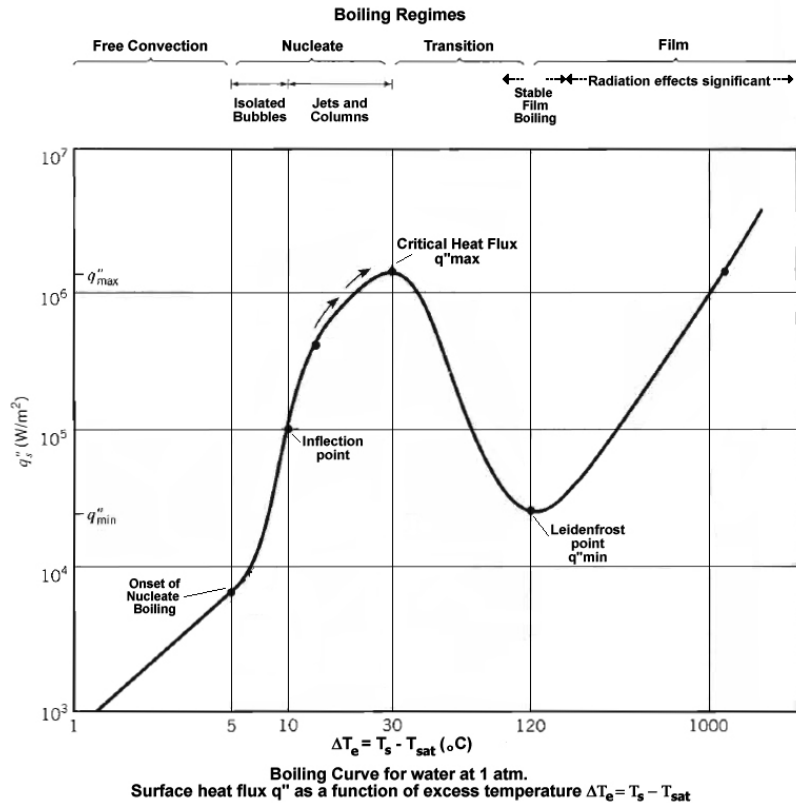


Figure 4.25: Boiling curve showing heat flux regimes, onset of nucleate boiling, and critical heat flux (CHF). From Wikipedia<sup>5</sup>

Simulating both nucleate boiling and ordinary convection is challenging, so nucleate boiling was not included in the FLUENT boundary conditions. As a result, the CFD results are conservative and may underestimate the actual heat transfer.

**Chamber Wall:** The goal is to determine the hot-gas wall temperature from CFD ( $T_{wg, CFD}$ ) and compare it to the set value from the cooling reservoir. For the same heat flux,  $T_{wg, CFD}$  should be lower than or equal to the set temperature, indicating that the cooling channel works properly.

**Coolant Transport Properties:** The objective is to ensure the pressure drop in the channels is within the range that the pressure-fed system can compensate for, and that the coolant can effectively absorb heat from the combustion chamber wall.

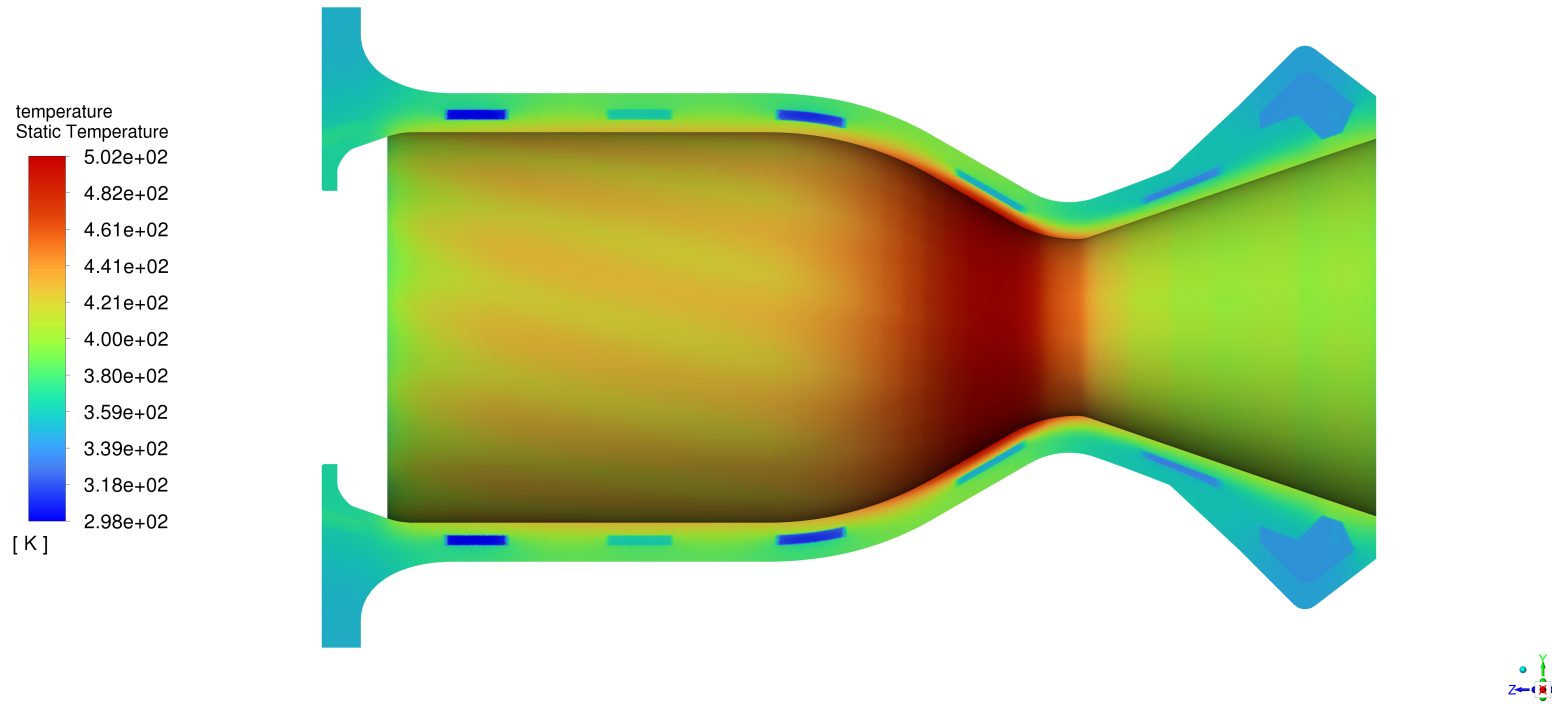


Figure 4.26: Hot-gas wall temperature, *side* cross-sectional view from CFD simulation.  
The heat flux boundary condition is obtained from RPA with an ideal cooling reservoir at  $T_{CO\infty} = 516.15\text{K}$  ( $243^\circ\text{C}$ ), and  $T_{wg, \text{baseline}} \approx 250^\circ\text{C}$

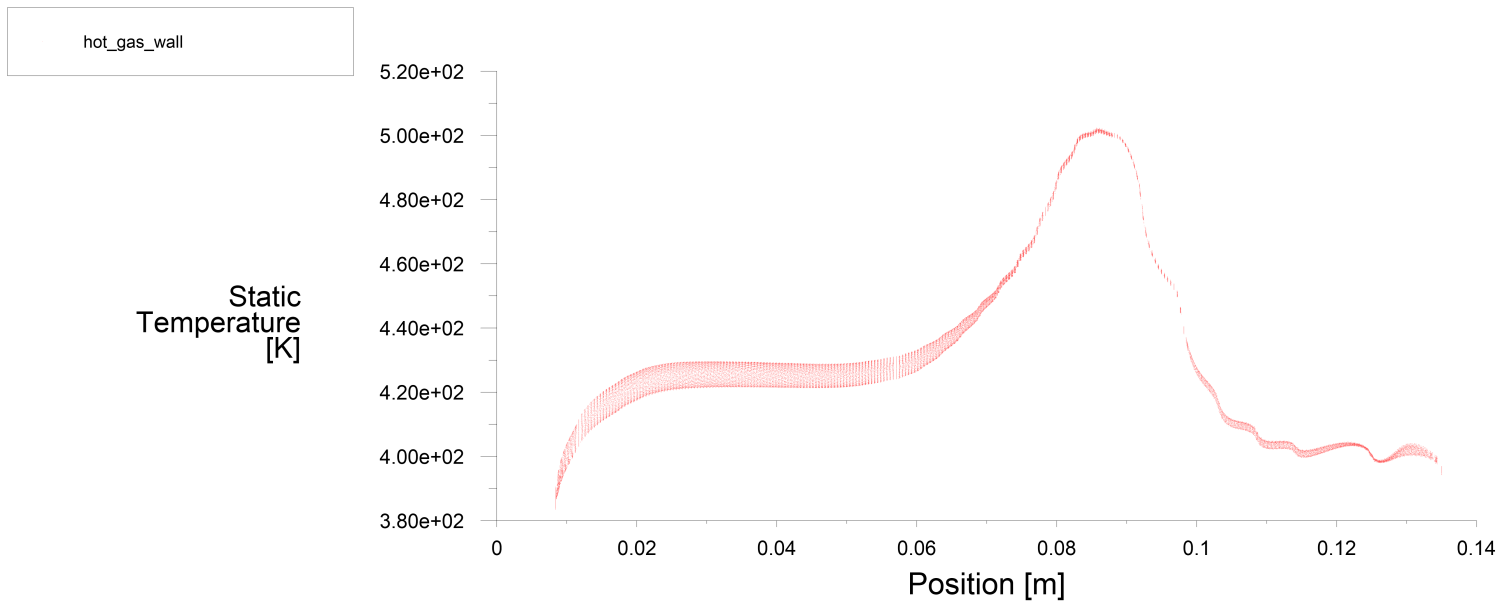


Figure 4.27: Wall temperature along the centerline axis from CFD simulation.

Due to double-pass cooling, the temperature is bounded by distinct upper and lower curves.

The temperature at the end of the nozzle is jerky due to the extra manifold volume at the end of the expansion nozzle.

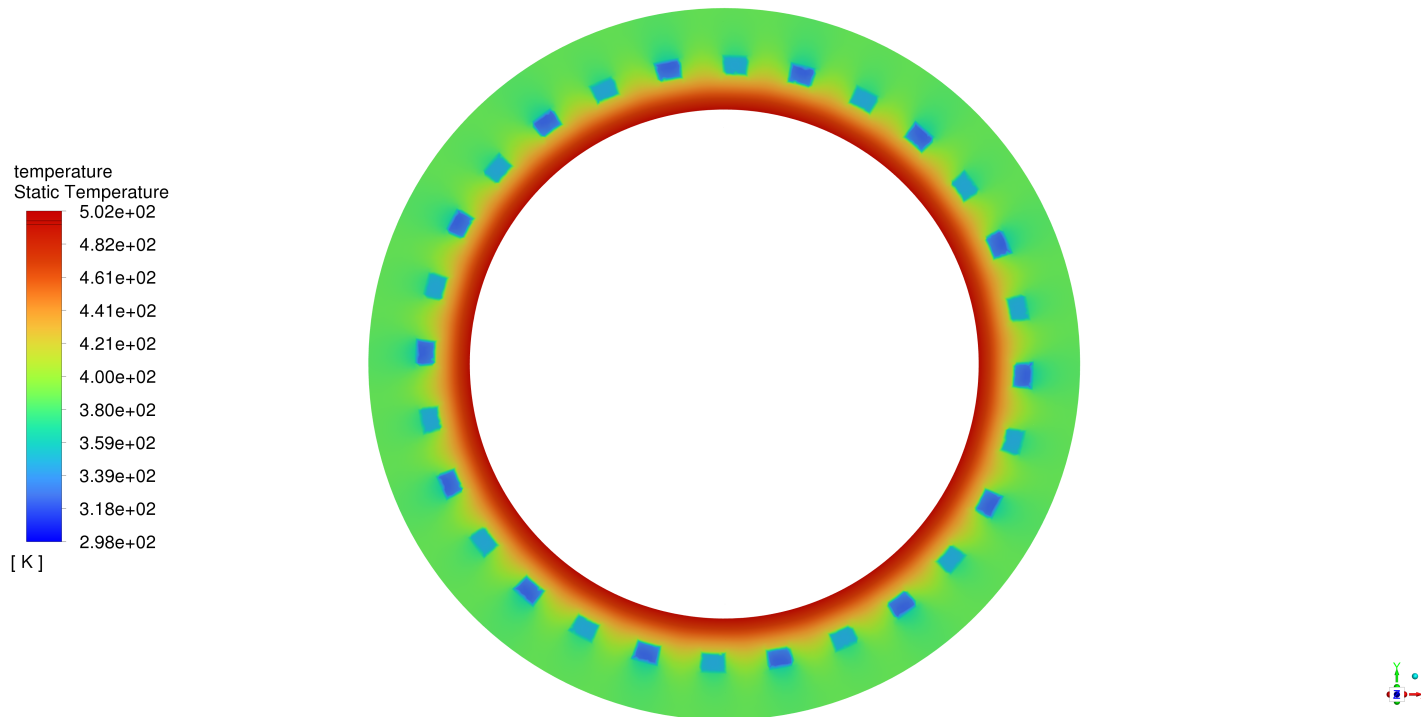


Figure 4.28: Hot-gas wall temperature, *throat* cross-sectional view from CFD simulation.  
The heat flux boundary condition is obtained from RPA with an ideal cooling reservoir at  $T_{CO \infty} = 516.15\text{K}$  ( $243^\circ\text{C}$ ),  
and  $T_{wg, \text{baseline}} \approx 250^\circ\text{C}$

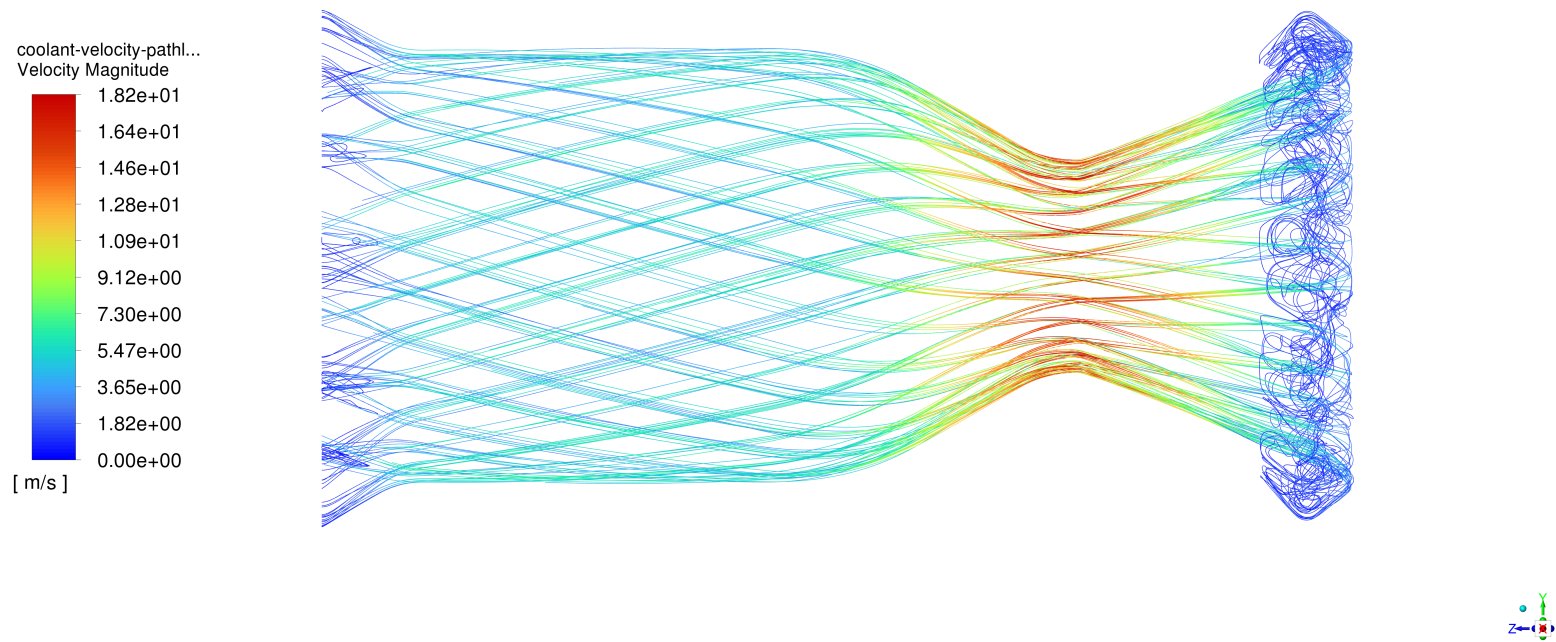


Figure 4.29: Coolant velocity pathlines from CFD simulation.

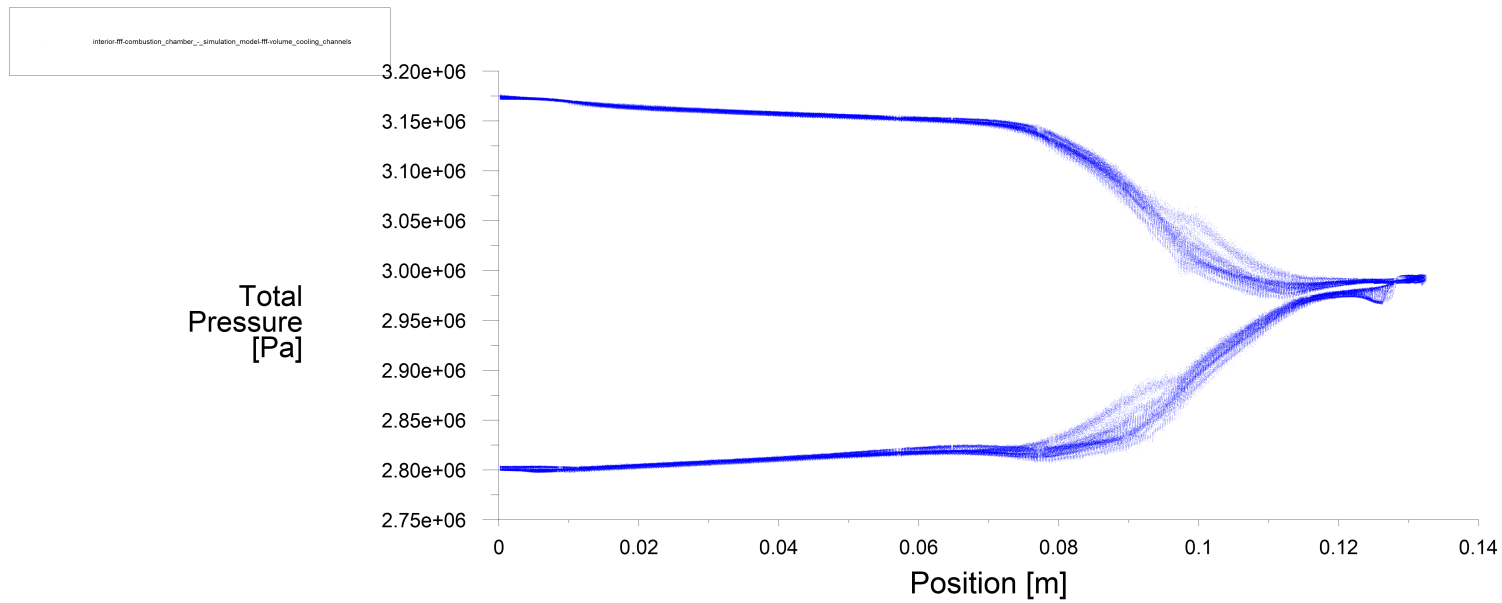


Figure 4.30: Coolant pressure distribution along centerline axis.

Around the throat area, the pressure distribution spreads out due to highly turbulent flow, which helps with cooling at the throat area.

From the CFD results:

- Wall temperatures remain below 250°C throughout the chamber: approximately 160°C in the cylindrical section, 230°C at the throat, and 130°C at the nozzle exit. This confirms that the cooling channel design is effective.
- A significant thermal gradient is observed at the throat section, which is a common issue in regeneratively cooled rocket engines and will be discussed further in Section 4.4.
- The variable cross-sectional cooling channels help maintain distributed flow velocities, with about 7 m/s in the cylindrical section and 18 m/s at the throat.
- The pressure drop across the cooling circuit is about 3.5 bar, which is higher than expected but still within the margin for the pressure-fed system.

These results demonstrate that the hot-gas wall temperature remains below the set limit of 250°C, determined by the chamber material's maximum operating temperature. This ensures the chamber does not exceed its safe temperature limit during operation.

Numerically, the expected wall temperature ranges are:

$$T_{wg, \text{cylindrical section, CFD}} \in [153^\circ\text{C}, 250^\circ\text{C}]$$

$$T_{wg, \text{throat, CFD}} \in [229^\circ\text{C}, 250^\circ\text{C}]$$

$$T_{wg, \text{exit, CFD}} \in [127^\circ\text{C}, 250^\circ\text{C}]$$

### Final verdict

Critical Heat Flux Analysis 4.3.5 shows that, at a hot-gas wall temperature of 200°C (within 30K above the saturation temperature at 21 bar), the maximum heat flux is 6.5 MW/m<sup>2</sup>, which is well within the nucleate boiling regime for ethanol. This means the engine wall temperature is effectively bounded between 183°C and 213°C.

CFD-based Convection Heat Transfer Analysis 4.3.5 confirms that, with a set hot wall temperature of 250°C, the cooling circuit maintains actual wall temperatures well below the material limit, with typical values down to 225°C or lower depending on the chamber section.

In summary, the chamber wall temperature is safely bounded by the nucleate boiling regime and the cooling circuit performance, ensuring reliable operation within the materials' safe temperature range.

### 4.3.6 Final cooling configurations

#### Summarization of Design points

Design point	Value
Coolant	Ethanol
Coolant mass flow rate	0.20 kg/s
Cooling circuit architecture	Double pass cooling circuit
Number of channels <sup>6</sup>	28
Cooling channels size at	<ul style="list-style-type: none"> <li>• cylindrical section: <math>1.5 \times 2.5</math> mm</li> <li>• throat: <math>1.2 \times 1.0</math> mm</li> <li>• end of divergence section: <math>2.0 \times 2.2</math> mm</li> </ul>
Helical angle	$25^\circ$
Film cooling	14 holes of 0.3 mm diameter

Table 4.4: Design Points for Regenerative Cooling Circuit.

## 4.4 Structure Analysis

The body temperature and pressure inside the cooling channels are imported from the FLUENT CFD simulation into Ansys Mechanical for thermal and structural coupled analysis. The boundary conditions are as follows:

- Environmental temperature:  $22^\circ\text{C}$ , which is the temperature from which the shape of the part is derived in CAD
- Material: AlSi<sub>10</sub>Mg, with temperature-dependent material properties
- Structural load: internal chamber pressure profile from nozzle expansion calculations; cooling channel pressure from CFD simulation
- Thermal load: body temperature profile from CFD simulation

From the simulations, the MCC generally has very low stress. Compared with AlSi<sub>10</sub>Mg  $\approx 158$  MPa yield strength at  $200^\circ\text{C}$ , most of the chamber is well below that yield strength value, usually within *Safety Factor* of 2. However, a localized high-stress region is observed at the throat area due to the **doghouse effect**, which is discussed in detail later in this section.

---

<sup>6</sup> total of both passes

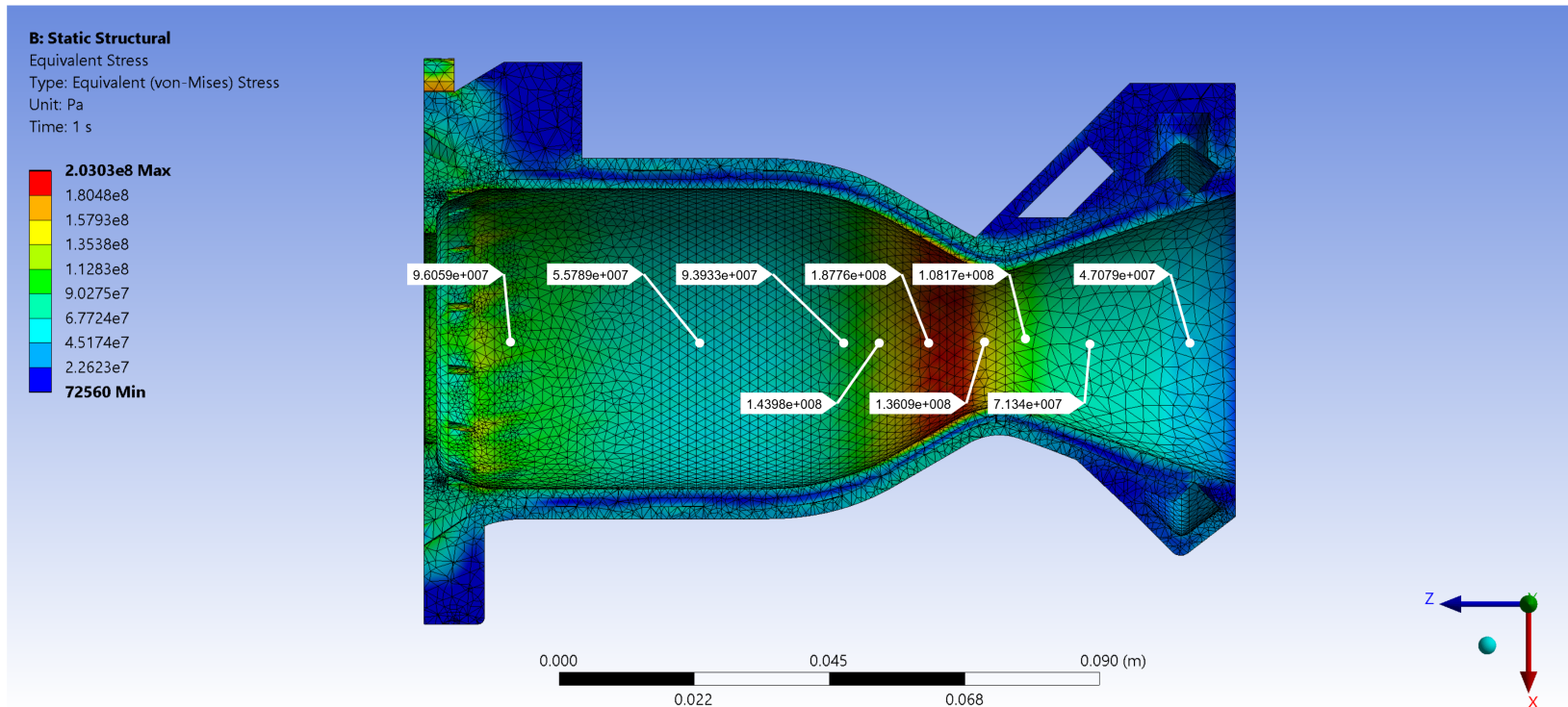


Figure 4.31: Thermal and structural coupled analysis of the BROKE 2 chamber showing temperature distribution and von Mises stress. The mesh shown contains approximately 300,000 nodes; validation with a refined mesh of 1,800,000 nodes yielded similar results, confirming mesh independence.

### Doghouse effect

The *doghouse effect* refers to a localized region of elevated thermal and mechanical stress that forms at the outermost hot-gas wall elements near the throat of a regeneratively cooled rocket engine. This region is particularly susceptible to plastic deformation and fatigue due to the combined effects of high heat flux, steep temperature gradients, and structural constraint.

In this analysis, the chamber is made of AlSi<sub>10</sub>Mg. At the operating temperature of 200°C, the material yield strength is approximately 158 MPa. The FEA simulation shows a von Mises stress of 183 MPa at the outermost node in the throat region, indicating that the wall is at or just above the yield threshold. The outer hot-gas wall will deform plastically.

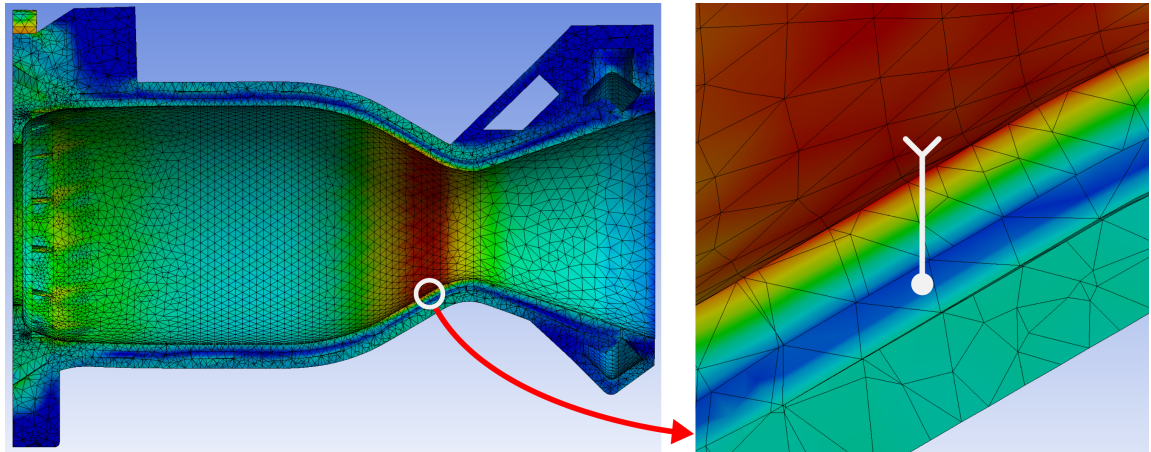


Figure 4.32: Doghouse effect. The direction of the arrow is the direction of positive Distance along the path.. While the walls only have 4 nodes, there seem to be many more datapoints due to Ansys' internal interpolation.

The doghouse effect can be clearly observed from this simulation. Due to resource constraints, the analysis was run with adaptive mesh with an average characteristic length of 0.25 mm for fast result iterations. Although the detailed FEA cross-section view shows that the path only crosses 4 mesh nodes, Ansys Mechanical interpolates the results between these nodes, resulting in a plot with more data points than the mesh would suggest.

Later on, higher mesh resolution runs were performed as *mesh sensitivity analysis*, by increasing the node counts from 300,000 nodes to 1,600,000 nodes. The values are nearly identical, and hence the model can be considered to be *mesh insensitive*. Moreover, the linear trend observed in the plot 4.33 is consistent with theory: according to Fourier's law of heat conduction, a fixed cooled boundary and a linear thermal gradient produce a linear thermal stress gradient. This agreement between simulation and theory supports the physical interpretation of the quick-but-coarse results.

The doghouse phenomenon is not unique to the BROKE engine, but is a well-known lifetime limitation for all regeneratively cooled rocket engines. The doghouse effect is a primary factor in determining engine durability and service life, as the high stress concentrations can lead to crack initiation and fatigue under cyclic thermal and mechanical loading.

However, the aspect of lifetime assessment is beyond the scope of this thesis. Due to limited

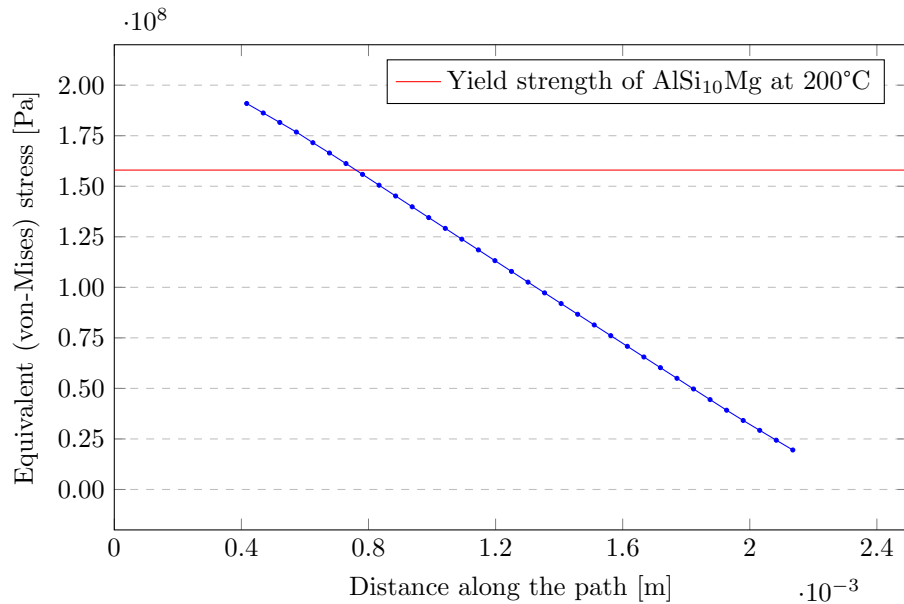


Figure 4.33: Thermal stress of hot-gas wall at the throat along the path



Figure 4.34: Doghouse effect cross-section[10]

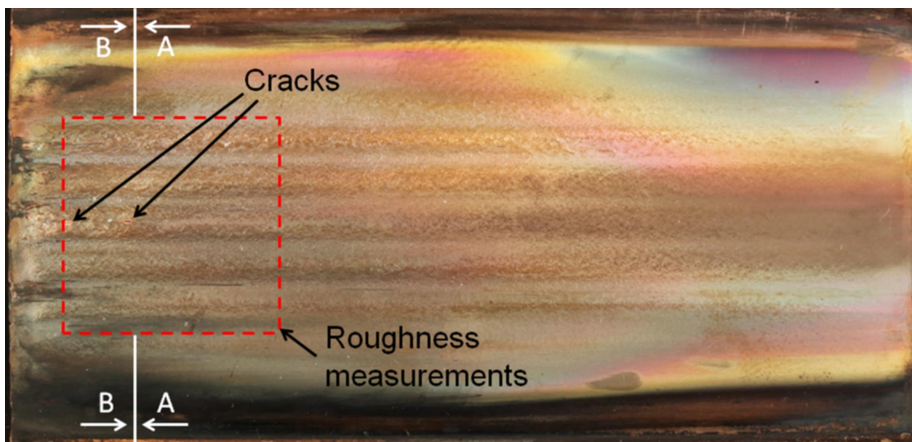


Figure 4.35: Doghouse effect streaks on the chamber wall[10]

resources, the doghouse effect is not mitigated in this design. For future lifetime assessment, the Porowski Beam Model and Finite Element Analysis (FEA) can be used to predict the lifetime of the chamber.

At this stage, the doghouse effect is a localized stress concentration at the throat and does not compromise overall strength. The surrounding wall remains below the temperature-dependent yield limit of AlSi<sub>10</sub>Mg, indicating safe operation within the design envelope. Further hot-fire testing and inspections are needed to confirm material behavior, but current analysis suggests the chamber should last well beyond a few firing cycles.

## 4.5 Design-for-Manufacturing Features

To facilitate the manufacturing process of the BROKE 2 MCC using SLM, several design-for-manufacturing (DfM) features were incorporated into the design. These features aim to optimize depowdering and fixturing during post-processing on Subtractive Machining.



Figure 4.36: DfM features in BROKE 2 MCC, green arrow indicates printing orientation:  
 (1) Clamping surface for 4-jaw chuck, (2) Depowdering ports

## 4.6 Final Main Combustion Chamber Design

After extensive design iterations, analysis, and validation, the final configuration of the BROKE 2 main combustion chamber was realized. The following figures illustrate the completed chamber, showcasing its key features and manufacturing details.



Figure 4.37: Final BROKE 2 Main Combustion Chamber Side View



Figure 4.38: Final BROKE 2 Main Combustion Chamber Top View

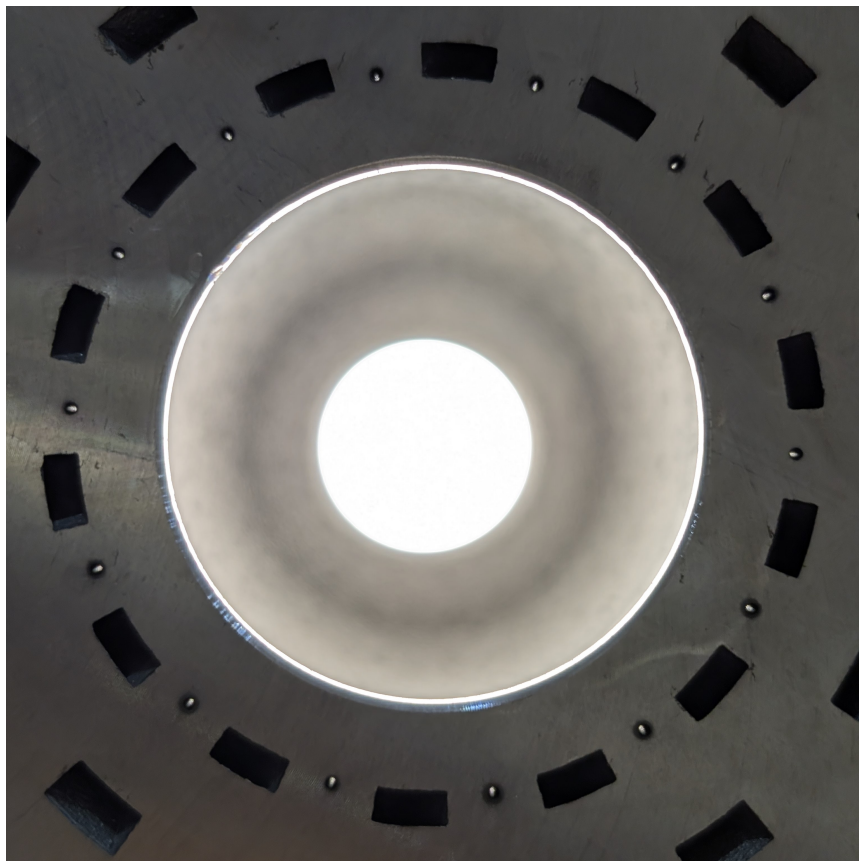


Figure 4.39: Final BROKE 2 Main Combustion Chamber Film Cooling Ports

This page is intentionally left blank.

# Chapter 5

## Final Conclusion

This thesis has detailed the design, analysis, and manufacturing of the BROKE 2 liquid rocket engine, with a focus on balancing technical performance against practical constraints such as budget, manufacturability, and available resources. The project demonstrated the feasibility of additive manufacturing for critical engine components, particularly the main combustion chamber, and emphasized the importance of regenerative cooling in small-scale rocket engines.

Key design choices—including the selection of AlSi<sub>10</sub>Mg for the chamber material and the implementation of double-pass, helical cooling channels—were validated through empirical analysis and CFD simulations. The cooling system maintained safe wall temperatures and addressed the square-cube scaling challenges inherent to small engines. Structural analysis confirmed that the chamber design remains within material limits, with the doghouse effect recognized as a critical factor for long-term durability.

Throughout the project, valuable lessons were learned regarding the limitations and advantages of additive manufacturing, the importance of design-for-manufacturing features, and the need for iterative validation through test prints and simulation. The modular subsystem approach adopted for the engine architecture ensures maintainability and future adaptability.

Ultimately, the BROKE 2 engine serves as a successful demonstration of student-driven rocket engine development, providing insights for future projects and contributing to the broader field of small-scale propulsion research.

**Due to the thesis submission deadline, I was unable to include detailed documentation for all engine components, although they have been designed and manufactured. Testing is scheduled after submission, and I hope to present the results in a future revision. Design validation through testing will further strengthen this work, and I hope this thesis serves as a useful reference for students pursuing rocket engine development.**

In the end, it is engineering, and risks must be taken ^\\_\(')\\_/-

This page is intentionally left blank.

# Bibliography

- [1] Sebastien Dryepondt et al. “Microstructure and high temperature tensile properties of 316L fabricated by laser powder-bed fusion”. In: *Additive Manufacturing* 37 (2021), p. 101723. ISSN: 2214-8604. DOI: <https://doi.org/10.1016/j.addma.2020.101723>. URL: <https://www.sciencedirect.com/science/article/pii/S2214860420310952>.
- [2] Naor Elad Uzan et al. “High-temperature mechanical properties of AlSi10Mg specimens fabricated by additive manufacturing using selective laser melting technologies (AM-SLM)”. In: *Additive Manufacturing* 24 (2018), pp. 257–263. ISSN: 2214-8604. DOI: <https://doi.org/10.1016/j.addma.2018.09.033>. URL: <https://www.sciencedirect.com/science/article/pii/S2214860418302148>.
- [3] George P. Sutton and Oscar Biblarz. *Rocket Propulsion Elements - 9th Edition*. Wiley, 2016.
- [4] Dieter K Huzel and David H Huang et al. *Modern Engineering for Design of Liquid Propellant Rocket Engines (Progress in Astronautics and Aeronautics)*. AIAA (American Institute of Aeronautics & Astronautics), 1992.
- [5] Samuel Stein. *A high-performance 250-pound-thrust rocket engine utilizing coaxial-flow injection of JP-4 fuel and liquid oxygen*. URL: <https://hdl.handle.net/2027/uiug.30112106742346>.
- [6] Mike Jetzer. *F-1 Thrust Chamber*. URL: <http://heroicrelics.org/info/f-1/f-1-thrust-chamber.html>.
- [7] Welt. *Rocket Science - The success story of Ariane 5 (Pt 1) | Full Documentary*. URL: <https://youtu.be/Rw1A-HcQExA>.
- [8] Ian H. Bell et al. “Pure and Pseudo-pure Fluid Thermophysical Property Evaluation and the Open-Source Thermophysical Property Library CoolProp”. In: *Industrial & Engineering Chemistry Research* 53.6 (2014), pp. 2498–2508. DOI: 10.1021/ie4033999. eprint: <http://pubs.acs.org/doi/pdf/10.1021/ie4033999>. URL: <http://pubs.acs.org/doi/abs/10.1021/ie4033999>.
- [9] Michael Meyer, Diane Linne, and Donald Rousar. “Forced convection boiling and critical heat flux of ethanol in electrically heated tube tests”. In: *36th AIAA Aerospace Sciences Meeting and Exhibit*. DOI: 10.2514/6.1998-1055. eprint: <https://arc.aiaa.org/doi/pdf/10.2514/6.1998-1055>. URL: <https://arc.aiaa.org/doi/abs/10.2514/6.1998-1055>.
- [10] Felix Hötte et al. “Experimental lifetime study of regeneratively cooled rocket chamber walls”. In: *International Journal of Fatigue* 138 (2020), p. 105649. ISSN: 0142-1123. DOI: <https://doi.org/10.1016/j.ijfatigue.2020.105649>. URL: <https://www.sciencedirect.com/science/article/pii/S0142112320301808>.



Scan to access the digital version of this document